arXiv:astro-ph/0101203v2 13 Jan 2001

ACCRETION AND EMISSION PROCESSES IN AGN

S. COLLIN
Observatoire de Paris-Meudon, 92195 Meudon, France
E-mail: suzy.collin@obspm.fr

The UV-X continuum, the X-ray spectral features, and the variability in these bands provide powerful tools for studying the innermost regions of AGNs from which we gain an insight into the accretion process. In this chapter the discussion focusses on luminous AGN, i.e. Seyfert galaxies and quasars. The standard accretion disk model (a stationary geometrically thin disk) is described, and vertically averaged solutions for the radial structure are given. The emission of the standard disk is discussed using different approximations, and it is compared to the observations. This leads to the conclusion that more complex models are required, such as the irradiated disk and the disk-corona models. The advantage of this last model is that it explains the overall UV-X spectral distribution. In the framework of these disk models, the profile, intensity, and variability properties of the X-ray iron line can be explained by reprocessing at the surface of the cold disk very close to the black hole (the "relativistic disk model"). An alternative possibility is discussed, where the UV-X continuum is produced by a quasi-spherical distribution of dense clouds surrounded by (or embedded in) a hot medium. In such a model the iron line profile could be due to Comptonization instead of relativistic effects.

1 A Few Introductory Words

In these lectures, I adopt the "black hole paradigm", in which AGN are fueled by accretion onto a massive black hole (BH)[100]. Besides the BH paradigm, there is another generally accepted model, i.e. that accretion takes place via a disk. A few initial comments should be made concerning this point.

One tries to account for AGN luminosity by invoking accretion with angular momentum. If the flow is rotationally supported, it will form a disk. The presence of a disk is inferred from several observational facts. The most obvious one is the existence of a privileged direction: several active galaxies display cones of ionized gas, and collimated jets are commonly observed in radio-loud objects, as well as in a few radio-quiet ones. The "Unified Scheme"[8] implies the existence of a dusty torus. Double peaked line profiles observed in a small fraction of AGN are also believed to be the signature of disk emission. Finally, large gaseous disks have been observed in some cases, for instance in NGC 4258. However, one should keep in mind that all these evidences point towards the existence of a disk *at large distances*, i.e. at $R \gtrsim 10^4 R_{\rm G}$ ($R_{\rm G} = GM/c^2$ is the gravitational radius, where M is the BH mass), while the bulk of the accretion luminosity is emitted by a very small region, at $\sim 10 R_{\rm G}$.

Figure 1. Schematic view of an AGN, showing the dimensions of different regions in $R_{\rm G}$ (and in pc for $M = 10^8$ M$_\odot$). The present chapter deals with the region located inside the "gravitationally unstable" part of the disk, closer than a few $10^3 R_{\rm G}$ from the BH.

At such small distances the only evidence for an accretion disk is the profile of the Fe K line. Since this issue is important (as it implies the presence of a "cold disk" at only a few $R_{\rm G}$ in some cases), one should question this "proof", and examine whether there is not another possible interpretation. Moreover, there are some theoretical hints for quasi-spherical accretion. For these reasons I discuss quite extensively the "quasi-spherical" model, which does not preclude the presence of angular momentum, although this is presently not a popular model.

In order to show the physical scale of the region discussed in this chapter, Fig. 1 displays a very schematic representation of the central flow in an AGN. We shall deal with the region located inside the "gravitationally unstable" part of the disk, closer than a few $10^3 R_{\rm G}$ (the distance where the broad lines are formed). There is presently no model proposed for the locally unstable region indicated in the figure, as the gravitational torques discussed in F. Combes' lectures concern the outermost parts of the nucleus, beyond 10 pc.

I have chosen to discuss extensively the most simple models, and to mention only briefly the recent more sophisticated developments. My aim is also to stress the uncertainties underlying some widely accepted and fashionable models. Finally I should mention that I focus on radio-quiet objects, where accretion processes dominate the spectrum.

The observational evidence is summarized in Sec. 2, and the basic physics of BHs are given in Sec. 3. In Sec. 4 a few results on the physical state of the medium emitting the bulk of the accretion power are deduced directly from the observations. In Sec. 5, the basis of accretion disk theory is recalled, emphasising some robust results concerning the emission spectrum, which are almost independent of the model. In Sec. 6, the standard (i.e. thin and steady) α-disks are discussed in their simplest (vertically averaged) form. Sec. 7 is devoted to the vertical structure. Sec. 8 tackles different models of "irradiated" disks, and their emission spectrum. Sec. 9 discusses the "cloud model", which is an alternative to these disks. In Sec. 10 the "thick" disk models envisioned for very low and very high accretion rates are briefly recalled. Sec. 11 reminds us that all this chapter deals with regions close to the BH, and that the accretion process is still not understood on larger scales.

Figure 2. Typical AGN continuum of radio-loud and radio-quiet objects, and possible emission mechanisms (some of them not mentioned in the text). Figure adapted from Koratkar & Blaes[57], ©1999, Astr. Soc. of the Pacific, reproduced with permission of the editors.

Figure 3. Mean line profile of the Fe K line for a sample of Sy 1 nuclei. The solid line is a double-Gaussian fit to the profile. From Nandra et al.[89].

2 Summary of Observations

I give here a very brief summary of some basic observational results which are crucial to constrain a model of the central engine. For more details the reader is referred to Koratkar & Blaes' excellent review[57].

2.1 The Broad-Band Spectrum

Fig. 2 displays a typical broad-band continuum, from the radio to the γ-ray range, for radio-quiet and radio-loud AGN[112]. The continuum in radio-quiet objects can be divided into three parts: an "IR-bump", a "UV-bump" (creating a gap at about 1μm), and an X-ray power-law continuum. The "1μm gap" is clearly due to the superposition of two different components which dominate the IR and the UV emission, and fade at 1μm. Since 1μm is the shortest wavelength at which hot dust can radiate, the IR-bump is attributed to hot dust radiation, at least in radio-quiet objects.

The continuum produced directly by accretion processes is restricted to the UV-X range (though the mid-IR continuum could be partly reprocessed nuclear radiation). From 1 to 10 eV the spectral index α, defined as $F_\nu \propto \nu^{-\alpha}$, lies in the range from -0.3 (for luminous quasars) to $+0.5$ (for Seyfert galaxies and low luminosity quasars). The soft X-ray continuum below 1 keV seems to be simply the extension of the UV with a spectral index close to 1.5. The continuum from 1 eV to about 100 eV is known as the *Big Blue Bump* (BBB), with a peak at 10 eV (see Fig. 5 in H. Netzer's chapter). A noticeable fact concerning the UV continuum is the almost complete *absence of a Lyman discontinuity* (a weak absorption edge is sometimes observed but it is most probably due to the Broad Line Region or to intervening intergalactic clouds with a redshift close to the emission one). I will not discuss here the "Warm Absorber", which imprints features in the soft X-ray continuum, as it

is covered in H. Netzer's lecture notes.

Above 1 keV the average spectral index is about 0.7, so that in the majority of objects the continuum below 1 keV shows a "soft X-ray excess" when compared to the extrapolation of the continuum in the 1-10 keV range. Recent observations performed with Chandra show that the strength of the excess has probably been overestimated in the past. Above 1 keV the spectrum can be decomposed into an underlying power-law with a spectral index (in photon number) $\Gamma \sim 1.9$ and, superimposed on it, a broad emission line peaking at 6.4 keV, identified with the Kα line of weakly ionized iron, and a "hump" peaking at about 30 keV (for a review see Mushotzky et al.[86]). It has been shown[132] that the strength of the hump, measured by a parameter R, correlates with Γ. The power-law continuum has a cut-off with an e-folding energy of 50 to 300 keV.

The Fe K line displays an asymmetrical profile with an extended red wing and a smaller blue wing[89] (see Fig. 3). The presence of the broad red wing in the average spectrum has been recently questioned[133]. However in the two best studied objects, MCG-6-30-15 and NGC 3516, the red wing extends down to 4 keV. The strength of the line seems also to correlate with Γ [133].

Finally, another important result is that the BBB luminosity is larger than the hard X-ray luminosity, in particular in luminous quasars.

2.2 Variability Properties

Since B. Peterson focussed mainly on the optical-UV properties, it is necessary to recall briefly some aspects of X-ray variability relevant to this chapter.

A well established result is that the characteristic time variability in the UV scales with luminosity: in Seyfert galaxies it is typically of the order of a few days, while it is several months in high luminosity quasars. The X-ray flux varies more rapidly than the UV, with typical time-scales of hours for Seyfert galaxies.

The conclusions one can draw from correlations between continuum bands are complex and sometimes controversial. For instance, NGC 7469 shows variations in the UV and X-rays with similar large amplitudes but with a time-delay of the order of 2 days, the UV leading the X-rays at maxima. The X-ray flux displays in addition short term variations not seen in the UV[90]. Moreover, the X-ray spectral index seems to be correlated with the UV flux[91]. In NGC 3516 the delay between UV and X-bands is larger than 2 days[29]. In NGC 4051 no optical variations were observed during strong X-ray variations[25]. The UV variations drive the optical variations with a time-delay ≤ 0.2 days in NGC 4151[28], ≤ 0.15 days in NGC 3516[29], and ~ 1 day (but

increasing with wavelength[129,16]) in NGC 7469. Soft X-ray variations are generally larger than hard X-ray ones, but this is not always the case[89]. In NGC 3516, they were strongly correlated with no measurable lag (≤ 0.15d)[29].

The centroid energy, the intensity, and the equivalent width of the Fe Kα line, are variable on short time-scales (down to ks). Correlations between the continuum and Fe K have been intensively looked for in a few objects with ASCA, RXTE, and now with Chandra, revealing a complex behavior (for a review see Nandra[88]). ASCA has observed rapid (1 to 10 ks) variations of Fe K in profile and intensity in MCG-6-30-15[51]. This result has been questioned[67,14] by recent observations of MCG-6-30-15 and NGC 5548 with RXTE, which show that the line flux is constant over time-scales of 50 to 500 ks, while the profile is variable and the underlying continuum displays large flux and spectral variations! The same result seems to be observed in NGC 3516. Reynolds[101] excludes a time-delay of 0.5 to 50 ks between the line and the continuum, and suggests that the line flux remains constant on time-scales between 0.5 and 500 ks in MCG-6-30-15. An analysis of a sample of Seyfert nuclei from the ASCA archive[130] finds that in most cases changes in the line do not appear to track changes in the continuum. Unfortunately, the new results found with Chandra are not yet published at the time of writing these lectures.

We summarize here the most important points that any model should be able to explain:

- Spectral features:
  - the overall shape of the continuum: the BBB (but does it include or not a soft X-ray excess?), the absence of the Lyman discontinuity, the UV/X ratio, the X-ray hump, the power-law, the break at ~ 100 keV, the Fe K line;
  - the correlation between R and Γ;
  - the very broad red wing of the iron line (at least in a few objects), and its centroid energy.
- Variability properties:
  - the rapid variations ($\leq$ ks) of the 2-10keV continuum;
  - the correlation between (and only between) long-term variations of UV and X-ray fluxes;
  - the very short (or absent) time-lag between optical and UV variations.

And perhaps a few other, but not so well established, variability properties: the slow variation of R; the rapid changes of the Fe K profile; and the absence of correlation of the Fe K flux with the underlying continuum.

Several other issues are not mentioned here, including the polarization properties, in particular, the abrupt increase of polarization level observed at 750 Å in quasars.

3 Black Holes, Accretion Rates, and Luminosities

It is beyond the scope of this chapter to discuss BH physics, for which excellent text books already exist[131,80]. For the purpose of this chapter it is only necessary to know that there are two types of BHs: non rotating or Schwarzschild BHs; and rotating or Kerr BHs. The innermost stable orbit of a Schwarzschild BH is equal to $6R_{\rm G}$, while it depends on the angular momentum, J, for a Kerr BH. Due to photon capture the maximum value of $cJ/GM^2 = 0.998$ and not unity, and it corresponds to a radius of the last stable orbit equal to $1.24R_{\rm G}$. Inside the innermost stable orbit, a particle falls almost radially onto the BH. The binding energy of the last stable orbit determines the efficiency of energy conversion. For Schwarzschild and Kerr BHs this is $\eta = 0.057$ and $\eta \sim 0.30$ respectively.

Another important parameter is the "gravitational redshift". This is due to the increase of proper-time with decreasing distance from the BH. Since $r = R/R_{\rm G}$ can be smaller for Kerr BHs, photons orbiting around a Kerr BH can be more redshifted than around a Schwarzschild BH.

The Eddington luminosity, $L_{\rm Edd}$, describes the maximum available power due to accretion. It corresponds to the equality between the gravitational force exerted on protons and the radiative force. In a fully ionized gas, the opacity is due to Thomson scattering, and this leads to the well known expression

$$L_{\rm Edd} = \frac{4\pi\ c\ GM\mu_e}{\sigma_{\rm T}} \quad , \tag{1}$$

where $\sigma_{\rm T}$ is the Thomson cross section and μ_e is the unit mass per electron. In units appropriate for quasars, this can be written as

$$L_{\rm Edd} = 1.5 \times 10^{46} M_8 \ \ {\rm erg\ s^{-1}} \quad , \tag{2}$$

where M_8 is the mass expressed in 10^8 $\rm M_\odot$. Note that this expression is valid in principle only for spherical accretion of a fully ionized medium in steady state.

The corresponding accretion rate is

$$\dot{M}_{\rm Edd} = \frac{L_{\rm Edd}}{c^2\eta} = 2.8\ M_8 \left(\frac{\eta}{0.1}\right)^{-1} \ \ {\rm M_\odot yr^{-1}} \quad . \tag{3}$$

Figure 4. T vs. Ξ for an optically thin medium exposed to a mixture of power-law continuum (of index 0.8 in F_ν) and a 10 eV BB, for increasing fractions of the BB intensity from top to bottom. From Nayakshin & Kallman[96].

We will often use the "Eddington ratio" $\dot{m} = \dot{M}/\dot{M}_{\rm Edd} = L/L_{\rm Edd}$. Some people define instead $\dot{m} = c^2\dot{M}/L_{\rm Edd}$, which differs by η from our expression.

B. Peterson showed in his lectures that BHs in Seyfert nuclei have a mass range of 10^7 to 10^8 $M_\odot$, with Eddington ratios of about 0.1.

4 What Does the BBB Tell us About the Emitting Medium?

The shape of the BBB implies thermal emission from an optically thick medium radiating as a black body (BB) at temperatures from a few 10^4K (optical emission) to a few 10^5K (EUV emission). The medium can however be optically thin at frequencies larger than the peak of the local Planck curve.

If the medium radiates like a BB, the size of the emitting region, $R_{\rm BBB}$, is given by

$$L_{\rm BBB} = {\rm Min}(1,\tau)\ a\ 4\pi R_{\rm BBB}^2\ \sigma T_{\rm eff}^4 \quad , \tag{4}$$

where $L_{\rm BBB}$ is the luminosity of the BBB, τ is the optical thickness, a is a factor of the order of unity that depends on the geometry of the emitting region (in the case of a disk $a = 0.5$), σ is the Stefan constant, and $T_{\rm eff}$ is the effective temperature. Since τ is larger than unity, using the definition of $R_{\rm G}$ one gets

$$r_{\rm BBB} = \frac{R_{\rm BBB}}{R_{\rm G}} \sim 30\ a^{1/2}\ T_5^{-2} M_8^{-1/2} \left(\frac{L_{\rm BBB}}{L_{\rm Edd}}\right)^{1/2} \quad , \tag{5}$$

where T_5 is the effective temperature in units of 10^5K.

One can deduce that the density of the emitting medium is high. Let us assume that the UV emitting medium "sees" the X-ray source, and that the surface layers are heated by this source. The temperature T of an X-ray heated gas, assuming a spherical geometry, is governed by a parameter Ξ defined as

$$\Xi\ \sim \frac{1}{n_e c k T}\ \frac{L_X}{4\pi R^2} \quad , \tag{6}$$

where $L_{\rm X}$ is the X-ray luminosity. Note that Ξ is closely related to the ionization parameter U used by H. Netzer in his lectures. The Ξ vs. T curve depends on the incident spectrum, as first shown by Krolik et al.[60]. This curve is characterized by two thermally stable solutions: a cool phase up to about 2×10^5 K, where the energy balance is due to atomic processes; and a hot phase close to the "Compton temperature" $T_{\rm Comp}$, that corresponds to the balance between Compton heating and Compton cooling. As an illustration, Fig. 4 displays the Ξ vs. T curves for an optically thin gas illuminated by a mixture of power-law continuum (index 0.8 for F_ν) and a 10 eV BB, for increasing fractions of the BB intensity. One can derive that the fraction of soft photons decreases with an increasing $T_{\rm Comp}$. For instance, the composite Laor et al[65] AGN continuum has $T_{\rm Comp} = 2.5 \times 10^6$ K, corresponding to the lower curve on the figure. We shall come back to the Ξ vs. T curve in the following sections. For the moment, we only need to know that whatever the fraction of BB emission, a temperature of 10^5K is obtained for $\Xi \sim 1 - 10$.

Since Ξ must be of the order of a few units, using Eq. (4) one gets:

$$n_e \sim 3 \times 10^{16}\ T_5^{-1}\ \ M_8^{-1}\ \left(\frac{L_{\rm X}}{L_{\rm Edd}}\right)\left(\frac{R}{10R_G}\right)^{-2}\ {\rm cm}^{-3}\ \ . \qquad (7)$$

Of course, things are more complicated if the medium is stratified and heated by non radiative processes, but this result remains basically correct.

The suggestion that this thick, dense, and relatively cold medium emitting the BBB could be identified with an accretion disk was made for the first time by Shields[115] for 3C 273, followed by subsequent papers[71,70]. There are however other alternative explanations which will be discussed at the end of the chapter. We now concentrate on the physics of "standard accretion disks" and their emission properties.

5 Thin Steady Accretion Disks: the Simplest Approximation

First we can show that *if the disk radiates like a BB at* $\sim 10^5 K$*, it is geometrically thin*, i.e. its scale height H is much smaller than its radius R. The vertical component of the gravitational acceleration at an altitude z is GMz/R^3, so $H \sim Rc_{\rm s}/V_\phi$, where $c_{\rm s}$ is the sound velocity and V_ϕ the orbital velocity. Although the temperature inside the disk can be (and actually is) larger than 10^5K, at 10-100$R_{\rm G}$ $c_{\rm s} \ll V_\phi$, which equals a fraction of the light velocity, so $H/R \ll 1$.

Since the disk is geometrically thin, the problem is reduced to two dimensions. The gas velocity has only two components, V_ϕ and V_r, the radial component. If the BH mass dominates the mass of the disk and the central

stellar cluster (which is the case for $R < 10^4 R_{\rm G}$), V_ϕ is Keplerian, so the orbital frequency $\Omega_{\rm K} = (GM/R^3)^{1/2}$, and one deduces the basic equation

$$H \sim c_{\rm s}\Omega_{\rm K} \quad , \tag{8}$$

which is a simplified form of the hydrostatic equilibrium equation.

At this stage we can determine the dynamical time $t_{\rm dyn}$, i.e. the time it takes for a perturbation to cross the disk vertically. According to Eq. (8),

$$t_{\rm dyn} \; = \; \frac{H}{c_{\rm s}} = \; \frac{1}{\Omega_{\rm K}} \quad , \tag{9}$$

which written in appropriate units gives

$$t_{\rm dyn} \sim 500 M_8 r^{3/2} \;\; {\rm s.} \tag{10}$$

This is the shortest time on which one can expect a change of structure to occur at a given radius.

The surface density, Σ, and V_r are governed by the continuity equation and the equation of motion:

$$\frac{\partial \Sigma}{\partial t} + \frac{1}{R}\frac{\partial}{\partial R}(R\Sigma V_r) = 0 \quad , \tag{11}$$

$$\frac{\partial}{\partial t}(R^2\Sigma\Omega_{\rm K}) + \frac{1}{R}\frac{\partial}{\partial R}(R^3\Sigma\Omega_{\rm K}V_r) = \frac{1}{2\pi R}\frac{\partial \mathcal{G}}{\partial \mathcal{R}} \quad , \tag{12}$$

where $\mathcal{G}$ is the torque between two adjacent rings.

To simplify the discussion, we consider a stationary disk. This is the case if the disk is fueled at a constant rate at its outer radius during the time it takes for the gas to reach the BH (the "viscous time"), and if there is no matter falling radially onto the disk at smaller radii. Instabilities can however suppress the stationarity. Under those conditions Eq. (11) becomes

$$\dot{M} = 2\pi R\Sigma V_r \quad , \tag{13}$$

where the accretion rate $\dot{M}$ is constant along the radius; and Eq. (12) becomes

$$\mathcal{G} = R^2\Omega_{\rm K}\dot{M} \; + \; {\rm constant} \quad , \tag{14}$$

which describes the constancy of the angular momentum flux. From Eq. (13) it is interesting to note that the thin disk assumption (i.e. $V_r \ll V_\phi$) implies a large value of the surface density,

$$\Sigma \sim 10^{22}\frac{1}{\eta}\frac{c}{V_r}\frac{\dot{m}}{r} \;\; {\rm g\ cm^{-2}}. \tag{15}$$

Since matter orbits in circles it requires a dissipation mechanism to lose energy and move towards the BH. The question is how to ensure accretion, or

Figure 5. Disk spectrum, assuming that the disk radiates locally like a BB. Boundary corrections were not taken into account. The index 2 and the exponential cut-off correspond to the Rayleigh-Jeans and to the Wien part of the spectrum respectively.

in other words: what is the torque $\mathcal{G}$? Microscopic viscosity is far too small, so one has to seek for a more efficient mechanism. Let us assume for the moment that there is a *local* unspecified viscosity.

The kinematic viscosity ν is related to the torque through the viscous stress tensor, giving the rate at which angular momentum is transported. For a thin disk, the only interesting coordinate of the stress tensor is

$$T_{r\phi} = \rho\nu R\frac{\partial\Omega_{\rm K}}{\partial R} \quad , \tag{16}$$

where ρ is the density. The torque is thus equal to

$$\mathcal{G} = \int Rd\phi \int RT_{r\phi}dz \;=\; 2\pi R^3\nu\Sigma\frac{\partial\Omega_{\rm K}}{\partial R} \quad . \tag{17}$$

Note that since $\partial\Omega_{\rm K}/\partial R$ is negative, the torque is negative, and angular momentum is transported outwards, as required for accretion to take place.

Finally, one can compute the rate of energy dissipated in the disk per unit surface, $D(R)$. According to our assumption of a local viscosity, the potential energy is transformed into heat, so we would get $2\pi D(R) = GM\dot{M}/R^3$. However, we also have to take into account the conservation of angular momentum and the fact that the torque cancels at $R_{\rm in}$, the radius of the last stable orbit. This leads to an extra factor $(3/2)(1-\sqrt{R_{\rm in}/R})$ (for a detailed demonstration see Krolik[59]). Finally one gets

$$D(R) = \frac{3GM\dot{M}}{4\pi R^3}f(R) \quad , \tag{18}$$

where $f(R) = (1-\sqrt{R_{\rm in}/R})$. In a fully relativistic treatment the expression of $f(R)$ would be more complicated. It is important to realize that the approximate R^{-3} dependence of the dissipation leads to a luminosity roughly proportional to $1/R$. Therefore, *the bulk of the gravitational energy is released close to the BH, at a few $R_{\rm G}$, but this does not mean that the bulk of the radiation necessarily comes from this region* (cf. the "cloud model").

If the disk radiates like a BB, the temperature $T_{\rm BB}$ is equal to the effective temperature $T_{\rm eff}$. Since the energy is radiated by both faces of the disk, $T_{\rm eff} = (D/2\sigma)^{1/4}$, which translates into

$$T_{\rm eff} \sim 6\times10^5\eta^{-1/4}f(R)^{1/4}\dot{m}^{1/4}M_8^{-1/4}r^{-3/4} \quad {\rm K}, \tag{19}$$

where $\dot{m}$ is defined by Eq. (3). Integrating the Planck function over the radius and neglecting the factor $f(R)$, one obtains the spectrum shown in Fig. 5, where $T_{\rm in}$ and $T_{\rm out}$ are the temperatures at the inner and outer radii. According to the Planck law, at a frequency $\nu = kT_\nu/h$, the regions with $T < T_\nu$, i.e. $R > R(T_\nu)$, contribute negligibly to the emission. On the other hand, in the inner regions where $T > T_\nu$, the spectrum at the frequency ν is given by the Rayleigh-Jeans expression $B_\nu = 2\nu^2 c^{-2} kT_{\rm eff}$. Thus, $L_\nu \propto \int_{R_{\rm out}}^{R(T_\nu)} R^{1/4} dR$, and finally *the emission at a frequency ν is dominated by material at the radius $R(T_\nu)$.*

This spectrum should be corrected for relativistic effects close to the BH, in particular in the case of a Kerr BH, where the inner radius is small. The effect is to make the spectrum dependent on the inclination angle, as L_ν is relativistically boosted towards high frequencies for edge on disks (cf. Fig. 12).

The fact that the bulk of the emission at a given wavelength is produced at the radius R_ν has important consequences for the variations of the different spectral bands. Since $B_\nu(T)$ peaks at $\lambda = 0.51/T({\rm K})$ cm, one deduces from Eq. (19), that the emission at λ_μ, expressed in microns, is produced mainly at a distance

$$r \sim 650\ \lambda_\mu^{4/3} \eta^{-1/4} f(R)^{1/4} \dot{m}^{1/4} M_8^{-1/4} \quad , \tag{20}$$

or

$$R \sim 1.2 \lambda_\mu^{4/3} \eta^{-1/4} f(R)^{1/4} \dot{m}^{1/4} M_8^{3/4} \ {\rm lt-d}. \tag{21}$$

From this we infer that the optical to near-UV emission corresponds to regions located at large distances from the BH. Comparing this result with the small time-delays between the UV and optical light curves (less than a fraction of a day), we see that it is marginally compatible with a causal link propagating at the speed of light. It is however incompatible with the dynamical time, according to Eqs. (10) and (20). But before we accept this conclusion we should question whether it is legitimate to assume that the disk is radiating locally like a BB, and therefore we have to obtain information on the optical thickness of the disk, and more generally on its physical properties. In this aim we have to specify the viscosity mechanism.

6 A Further Step: the α-Prescription, Vertically Averaged Models

6.1 Disk Structure

It is widely accepted that the mechanism for transportation of angular momentum can be identified with "turbulent viscosity" according to the "α-

prescription" proposed by Shakura & Sunyaev[113] (for a detailed discussion of α-disks see Frank et al.[33]). In this prescription it is assumed that the *sizes of the turbulent eddies are smaller than the thickness of the disk and that the turbulence is subsonic*, hence

$$\nu = \alpha c_{\rm s} H \quad , \tag{22}$$

where $\alpha \lesssim 1$.

The α-prescription has proven to give satisfying results when applied to disks in cataclysmic variables, where a relatively small value (≤ 0.1) of α is generally required. A magnetohydrodynamic instability pointed out by Chandrasekhar[13] is able to provide this viscosity[10]. Other prescriptions based on purely hydrodynamic (shear) instabilities are also under debate[105], in which the corresponding value of α can be larger and vary with $\Omega_{\rm K}$. The viscosity can be parameterized with a fixed Reynolds number[41,42,105], following an approach suggested already by Lynden-Bell & Pringle[69]. Finally the viscosity might also be a non-local mechanism, for instance in the case of an organized magnetic field anchored in the disk.

From Eqs. (13) and (14), one finds

$$V_r = \frac{3}{2}\alpha c_{\rm s}\frac{H}{R} \quad , \tag{23}$$

which shows that the radial velocity is strongly subsonic, and a fortiori strongly sub-keplerian, as expected.

The α-prescription is equivalent to the previous expression if *and only if* the disk is not self-gravitating. Eqs. (16) and (22) give

$$T_{r\phi} = \frac{3}{2}\alpha\rho c_{\rm s} H \Omega_{\rm K} \quad . \tag{24}$$

Using $c_{\rm s} = H\Omega_{\rm K}$, one gets

$$T_{r\phi} = \frac{3}{2}\alpha P \quad , \tag{25}$$

where P is the sum of the radiative and gas pressure.

If the ratio of the vertical component of the disk gravity to that of the central gravity, $\zeta = 4\pi G\rho/\Omega_{\rm K}^2$ is of the order of unity, then[48]:

$$c_{\rm s} = H\Omega_{\rm K}(1+\zeta)^{1/2} \quad \text{and} \quad T_{r\phi} = \frac{3}{2}\alpha P(1+\zeta)^{-1/2} \quad . \tag{26}$$

Actually there is a debate about the value of P one should take in the stress tensor: is it the total pressure or only the gas pressure? For the moment we adopt the use of the total pressure.

Because it is a matter of confusion, it is necessary to stress here that $T \sim T_{\rm mid-plane}$ and not $T_{\rm eff}$. If the diffusion approximation holds between the two temperatures, then $T \sim \tau^{1/4} T_{\rm eff}$, which implies that $T \gg T_{\rm eff}$ in the optically thick region.

All these expressions are *vertically averaged*. Since the disk is geometrically thin, these averaged quantities can be used to decouple the radial and vertical structures. Additional equations describe:

- The gas pressure:

$$P_{\rm gas} = \frac{\rho k T}{\mu m_{\rm H}} \quad , \tag{27}$$

  where μ is the mean mass per particle.

- The radiative pressure, which in the 2-stream approximation is given by

$$P_{\rm rad} = \frac{F_{\rm rad}}{c} \left[\frac{1}{2} \tau_{\rm R} + \frac{1}{\sqrt{3}} \right] \quad , \tag{28}$$

  where $\tau_{\rm R}$ is the Rosseland optical thickness of the disk.

- The flux radiated by each face of the disk[40]

$$F_{\rm rad} = \frac{4}{3} \frac{\sigma T^4}{\frac{1}{2}\tau_{\rm R} + \frac{1}{\sqrt{3}} + \frac{1}{3\tau_{\rm P}}} \quad , \tag{29}$$

  where $\tau_{\rm P}$ is the Planck optical depth. Note that, in the optically thick case, $P_{\rm rad}$ tends to its LTE value and $F_{\rm rad} \approx (8/3)\sigma T^4/\tau_{\rm R}$, which is the well-known diffusion approximation. In the optically thin case, $F_{\rm rad} \approx 4\sigma T^4 \tau_{\rm P}$.

- The energy balance between the local viscous dissipation and the radiative cooling,

$$F_{\rm rad} = D(R)/2 \quad . \tag{30}$$

These equations, when solved self-consistently with the appropriate functions for $\kappa_{\rm R}(\rho, T)$, $\kappa_{\rm P}(\rho, T)$ and $\mu_{\rm P}(\rho, T)$, yield the radial disk structure in the non self-gravitating region of the disk for given values of M, $\dot{M}$, and α. One finds that the disk is divided into several regions, according to the dominating processes: radiation or gas pressure; Thomson, Kramers, or more complicated opacity; and self-gravity or no self-gravity.

To show the importance of the opacity, Fig. 6 displays the radial dependence of several physical quantities as function of the radius for an α-disk

Figure 6. From left to right and top to bottom, density, surface density, Rosseland mean optical thickness, scale height, equatorial temperature and radiation to gas pressure ratio as functions of the radius for a vertically averaged α-disk. The thick solid line corresponds to a 2D model with realistic opacities. Courtesy of J.-M. Huré.

Figure 7. Transition from radiation to gas pressure regime for a vertically averaged α-disk, for $M = 10^8 \mathrm{M}_\odot$. The figure displays $\dot{m}$ versus r for different values of α. Courtesy of J.-M. Huré.

Figure 8. Transition to the self-gravity regime for a vertically averaged α-disk. The figure displays $R_{\rm sg}/R_{\rm G}$ versus $\dot{m}$ for different values of M. All models except one are computed for $\alpha = 0.1$. The curves are labelled with $\log M$ in units of $\mathrm{M}_\odot$.

in the case of a typical AGN. In these computations self-gravity has been neglected in order to focus on the other parameters. Different approximations have been compared to a 2D computation with realistic opacities. We see that in the inner region ($R \leq 10^{16}$ cm, i.e. $r \leq 10^3 R_{\rm G}$), the opacity is better approximated by Thomson scattering, while in the outer region it is better approximated by Kramers' opacity. Note that the radiation pressure dominates in the Thomson regime ($\beta = P_{\rm gas}/P_{\rm rad}$).

Fig. 7 shows that the transition between the radiation and gas pressure dominated regimes occurs at a larger radius for a larger accretion rate in Eddington units. This radius also increases with a decreasing viscosity parameter α, which corresponds to an increasing density. For a typical AGN ($\dot{m} = 0.1$ and $M = 10^8 \mathrm{M}_\odot$) and $\alpha = 0.1$, $R \sim 2000 R_{\rm G}$. Note that it occurs in the same region as the transition to the self-gravity regime (this is due to the rapid increase of density when the disk gravity begins to dominate).

Finally the disk becomes self-gravitating at a radius $R_{\rm sg}$ corresponding to $\zeta \sim 1$. As shown in Fig. 8, the transition occurs at $R \sim 100 - 1000 R_{\rm G}$. It is located further away for a larger value of α, owing to the corresponding smaller value of the density.

In summary *the non self-gravitating part of the disk is generally reduced to the Thomson opacity–radiation pressure dominated regime.* Neglecting the boundary function $f(R)$ the different parameters vary as:

- $\rho \propto R^{3/2}$,

- H = constant ,
- Σ and $\tau \propto R^{3/2}$,
- $T \propto R^{-3/8}$,
- $\zeta \propto R^{9/2}$,
- $P_{\rm gas}/P_{\rm rad} \propto R^{21/8}$.

These relations explain why the transition from the gas pressure to the radiation pressure regime, and the transition to self-gravity, are so rapid (see the strong variation of ζ and $P_{\rm gas}/P_{\rm rad}$ as functions of the radius on Fig. 7). It is also interesting to note that the gas temperature decreases less rapidly than $T_{\rm eff}$ (which is proportional to $R^{-3/4}$). The scale height to radius ratio can be expressed in this region as

$$\frac{H}{R} = 6.7 \frac{\dot{m}}{r} \quad , \tag{31}$$

which shows that the "geometrically thin" assumption does not hold for large $\dot{m}$; and the Thomson thickness is given by

$$\tau_{\rm T} \;=\; 55 \alpha^{-1} \left(\frac{R}{R_{\rm G}} \right)^{3/2} \quad . \tag{32}$$

A few important time-scales relevant to the external regions which emit at optical wavelengths, where self-gravity is not negligible, are defined below. The "viscous time" $t_{\rm visc}$, basically the time it takes for matter to move to the center, can be expressed as (using in particular Eq. (26)):

$$t_{\rm visc} \sim \frac{R}{V_r} \;\sim\; \frac{1}{\alpha} \left(\frac{H}{R} \right)^{-2} \frac{1}{\Omega_{\rm K} \sqrt{1+\zeta}} \quad . \tag{33}$$

The "thermal time" $t_{\rm th}$, i.e. the time it takes to radiate the thermal energy, can be expressed as

$$t_{\rm th} \;\sim\; \frac{PH}{D(R)} \;\sim\; \frac{\sqrt{1+\zeta}}{\alpha \Omega_{\rm K}} \quad . \tag{34}$$

The expression for the dynamical time $t_{\rm dyn}$ has already been given in Eq. (9). Correcting for self-gravity, it becomes

$$t_{\rm dyn} \;\sim \frac{1}{\Omega_{\rm K} \sqrt{1+\zeta}} \quad . \tag{35}$$

Figure 9. Viscously (left) and thermally (right) unstable regions for a vertically averaged α-disk, with $\alpha = 1$, $M = 3 \times 10^7 \mathrm{M}_\odot$, and $\dot{m}$=0.03. The figure displays T (in K) and H (in cm) versus r. The solid line represent the unstable regions. From Huré[45].

It is easy to see from these expressions that

$$t_{\rm visc} \gg t_{\rm th} \geq t_{\rm dyn} \quad . \tag{36}$$

For instance in the inner Thomson opacity - radiation pressure dominated region $t_{\rm visc}$ is given by

$$t_{\rm visc} = 10\ \alpha^{-1} M_8 \dot{m}^{-2} r^{5/2} \quad \mathrm{s}. \tag{37}$$

6.1.1 Stability of the Disk

There are 3 main instabilities acting in the disk:

1. the thermal instability, which occurs when
$$\left(\frac{\partial \ln D}{\partial \ln T}\right)_R - \left(\frac{\partial \ln F_{\rm rad}}{\partial \ln T}\right)_R > 0 \quad ; \tag{38}$$
2. the viscous instability, which occurs when
$$\left(\frac{\partial \ln \dot{M}}{\partial \ln \Sigma}\right)_R < 0 \quad ; \tag{39}$$
3. the gravitational instability, which occurs when[127,34]
$$Q = \frac{\Omega_{\rm K}^2}{\pi G \rho} < 1 \quad . \tag{40}$$

In the self-gravitating regime, where[46] $\rho \propto R^3$ and $\Sigma \propto R^2$, the disk shrinks, rapidly becomes strongly gravitationally unstable, and unstable fragments with a typical volume H^3 begin to collapse. Consequently, for $R > R_{\rm sg}$ the α viscosity does not hold. We stress that this gravitational instability is *local*, and does not require the disk mass to be of the order of the BH mass. The instability corresponds simply to the tidal limit $4\pi\Sigma \geq MH/R^3$, or equivalently to $M_{\rm disk} \sim MH/R$, hence $M_{\rm disk} \ll M$.

It can be shown that the thermal and the viscous instabilities are strongly linked, so they generally occur in the same region of the disk (see Fig. 9). We see that the disk is both viscously and thermally unstable in a large fraction

of the inner region. This combined instability should operate on a thermal time-scale, which is quite small in the inner regions (cf. Eqs. (10) and (34)). It should therefore induce rapid variations of EUV emission. Moreover as α-disks are also gravitationally unstable in the outer region, one deduces that *in AGN, α-disks are unstable almost everywhere!*

6.1.2 "β-Disks"

In the case where the stress tensor is assumed to be proportional to the gas pressure and not to the total pressure[15,78], the disks are known as "β-disks". Strictly speaking they should be called "$\alpha-\beta$-disks"! They are denser than α-disks, and dominated by gas pressure even in the inner regions. Consequently they are not subject to the viscous/thermal instability, but to another instability due to ionization of hydrogen, which occurs in regions where the mid-plane temperature is of the order of 10^4K. This instability induces a "limit-cycle" behavior, which is thought to explain the periodic variations of dwarf novae. In AGN it should operate on a much larger time-scale (10^5 yr), and could correspond to variations of 4 orders of magnitude in luminosity[120].

6.2 Where a Fundamental Ingredient, Compton Scattering, Appears

The solution of the vertically averaged disk showed that Thomson opacity dominates over free-free opacity in the inner regions. Diffusions are therefore important, and modify the equilibrium spectrum. Radiation is thermalized for a relatively small absorption optical thickness, when the effective optical thickness $\tau_{\rm eff} = \sqrt{\tau_{\rm abs}(\tau_{\rm abs}+\tau_{\rm T})} \sim \sqrt{\tau_{\rm abs}\tau_{\rm T}} > 1$, where $\tau_{\rm abs}$ and $\tau_{\rm T}$ are the absorption and diffusion optical thicknesses respectively. This occurs in the inner regions. In this case the spectral distribution is given by[111]

$$I_\nu = 2B_\nu\sqrt{\frac{\kappa_{\rm abs}}{\kappa_{\rm T}}} \ll B_\nu \quad . \tag{41}$$

For instance, if absorption is dominated by free-free processes,

$$\kappa_{\rm abs} = 3.69\times10^8 N_e N_i Z^2 g_{\rm ff}\frac{1}{\sqrt{T}}\frac{1}{\nu^3}\left(1-\exp\left(-\frac{h\nu}{kT}\right)\right), \tag{42}$$

and, using Eqs. (41) and (42), one deduces that the intensity is given by

$$I_\nu \propto \nu T^{1/4} \tag{43}$$

in the Rayleigh-Jeans regime, where $h\nu/kT < 1$; or

$$I_\nu \propto \nu^{3/2}\exp\left(-\frac{h\nu}{kT}\right)T^{-1/4} \tag{44}$$

in the Wien regime, where $h\nu/kT > 1$. The spectrum emitted by the innermost regions will therefore differ from a local BB.

However it is not sufficient to take into account Thomson scattering, as one can easily show that Compton scattering is also important. Since the gas temperature is high and we are interested in soft X-ray photons, the collisions between electrons and photons are not elastic, and they lose or gain energy with each scattering. The "Compton parameter" y, which is the total relative change of energy when a photon travels through the medium, is equal to the mean number of diffusions times the relative change of energy at each scattering. The mean number of diffusions, $N_{\rm s} = {\rm Max}(\tau_{\rm T}, \tau_{\rm T}^2) = \tau_{\rm T}^2$. In the case of a thermal non relativistic distribution of electrons, the relative change of energy at each scattering is given by[111]

$$\frac{\Delta h\nu}{h\nu} = -\frac{h\nu}{m_o c^2} + \frac{4kT}{m_o c^2} \quad , \tag{45}$$

and thus one gets

$$y = \frac{4kT - h\nu}{m_o c^2} \tau_{\rm T}^2 \quad . \tag{46}$$

In the inner regions of the disk, $\tau_{\rm T} \sim 10^4$ and $T \sim 10^6$K, so y can easily be larger than unity. If free-free dominates, then $\tau(\nu)$ and hence y increases with decreasing frequency, and there is a frequency ν_o below which $y > 1$. If $h\nu_o/kT \ll 1$, inverse Compton processes will drive soft photons to higher frequencies, and there will be an accumulation of photons at $\nu \sim 4kT/h$, at the expense of the low frequency population[22,128]. Another consequence of Compton diffusion is that the profile of a line will be asymmetrically broadened, as it is dominated by Inverse Compton diffusions for $\nu_{\rm line} < 4kT/h$, and by direct Compton diffusions for $\nu_{\rm line} > 4kT/h$ (i.e. down-scatterings leading to a broad red wing). The computation of the spectrum in this case is performed with transfer codes using the "Kompaneets diffusion equation", or with Monte Carlo codes. The effect of Compton scatterings on the spectral distribution of the disk is illustrated in Fig. 11, and at the end of the chapter we will discuss the effect on the profile of the iron line.

Another problem which has to be taken into account is the existence of an atmosphere above the disk. As a first approach[56,125], the disk was replaced by low gravity stellar atmospheres of different $T_{\rm eff}$. However, since gravity is constant in a stellar atmosphere, while it increases with height in disks, this method is not valid, and led to the erroneous result that the spectrum should always show a strong Lyman discontinuity in absorption.

Figure 10. Temperature and density structure of an α-disk for a typical AGN ($M = 10^8 \mathrm{M}_\odot$, $\dot{M} = 0.1 \mathrm{M}_\odot$ yr^{-1} or $\dot{m} \sim 0.03$, $\alpha = 0.1$). Courtesy of J-M. Huré.

7 The α-Prescription, Computation of the Vertical Structure and Vertical Transfer

The computation of an accurate emission spectrum requires a model of vertical structure with the self-consistent treatment of radiative transfer. Since the disk is still assumed to be geometrically thin, it is again possible to decouple the vertical and the horizontal structure equations. One then solves for each annulus a set of differential equations in z, instead of a set of algebraic equations. A simplification consists, at least in a first step, of decoupling the computation of the emitted spectrum from that of the vertical structure, as the disk is optically thick and the spectrum forms in the upper layers. The radiative transfer is then solved using the diffusion approximation.

7.1 Vertical Structure

The equations for the vertical structure are:

- the hydrostatic equilibrium,

$$\frac{1}{\rho}\frac{dP_{\rm tot}}{dz} = -\Omega_{\rm K}^2 z \quad ; \tag{47}$$

- the vertical variation of the energy produced by viscous dissipation,

$$\frac{dF}{dz} = \frac{9}{4}\rho\nu(z)\Omega_{\rm K}^2 \quad ; \tag{48}$$

- the variation of the mean optical thickness and of the surface density,

$$\frac{d\tau}{dz} = -\kappa\rho \quad \text{and} \quad \frac{d\Sigma}{dz} = \rho \quad , \tag{49}$$

  where κ is a frequency averaged opacity;

- the variation of the radiation pressure in the diffusion approximation, assuming that the energy is transported only via radiation,

$$-\frac{c_{\rm s}}{\mu\kappa}\frac{dP_{\rm rad}}{dz} = F(z) \quad . \tag{50}$$

A question is raised here: how is viscous heating deposited vertically? The original Shakura-Sunyaev prescription was introduced to describe vertically averaged quantities, and it is not clear how to extend it to a z-dependant model. According to the $\alpha - P$ prescription described above, it seems natural to assume that ν is constant vertically, which implies that the heat deposition dF/dz is proportional to ρ. If the opacity is dominated by Thomson scattering and the pressure is dominated by $P_{\rm rad}$, as is the case in the inner region of the disk, then Eqs. (47), (48) and (50) lead to the result that ρ does not depend on z. A different prescription is sometimes used for disks in dwarf novae[75].

Other ingredients can also be added to the model, such as convective transport. As an illustration, Fig. 10 displays the 2D structure of an α-disk, for $\alpha = 0.1$, taking into account convective and turbulent transport and self-gravity[47]. The parameters are those of a typical AGN ($M = 10^8 {\rm M}_\odot$, $\dot{M} = 0.1 {\rm M}_\odot/{\rm yr}$, or $\dot{m} \sim 0.03$). Comparing the results of 2D and 1D computations, one finds that the results are similar for the radial structure within factors of a few. The temperature in the equatorial plane is accurate to within 30% and the most important difference (by a factor ≤ 4) is in the disk thickness[49]. The density and the surface density, the critical radius for self-gravity, the ratio of gas to radiation pressure ratio are correctly computed in the 1D model (cf. Fig. 6). The 2D structure avoids however some multiple solutions met in the 1D model (cf. Fig. 9).

7.2 Disk Spectrum

Vertically averaged α-disks, which have proven to be extremely useful in determining the radial structure of the disk, are not sufficient to determine the emission spectrum. This requires solving the vertical radiative transfer in a consistent way with the vertical structure of the disk.

Several authors have built consistent models of the vertical structure of AGN accretion disks using various approximations for the radiative transfer. The first computation was performed by Laor & Netzer[64], who solved the radiative transfer in the Eddington approximation, with LTE, bound-free and free-free opacities, and with different assumptions for the stress tensor as well as for vertical heat deposition laws. They showed in particular that the Lyman discontinuity can appear either in absorption or in emission according to these laws. Ross et al.[107] relaxed the LTE assumption and took into account Comptonization using the Kompaneets equation. Störzer[123] solved the radiative transfer equation in 3D, also taking into account the influence of self-gravity, but keeping the LTE approximation. Shimura & Takahara[117,118] also solved the vertical structure together with the transfer treated with the

Figure 11. Spectrum of an α-disk around a Schwarzschild BH. Solid lines represent the contribution from different annuli and the total spectrum (with Componization). Dotted lines represent the local BB approximation used for the outermost annuli. Dashed lines represent the total spectrum with the local BB computation. From Ross et al.[108]

Kompaneets equation, but for a stress tensor proportional to the gas pressure and not to the total pressure. Störzer et al.[124] and Shields & Coleman[116], addressed the question of how departures from LTE influence the Lyman discontinuity. Dörrer et al.[26] solved the vertical structure self-consistently, with LTE and no bound-free opacities, and a pure-H atmosphere, but taking into account Compton scattering. Sincell & Krolik[122] solved the coupled vertical structure and radiation transfer with a two stream Eddington approximation, restricting the elements to He and H in LTE.

Fig. 11 illustrates the influence of Comptonization[107]. It shows the spectra of two (non-rotating) BHs, with different masses and accretion rates. This figure illustrates two interesting results:

1. The soft X-ray excess cannot be reproduced. Although a non-negligible fraction of the disk luminosity is radiated in the soft X-ray range as a consequence of Comptonization, it is obvious that the spectral energy distribution of AGN cannot be accommodated if one only assumes an extra power-law component exists in the soft X-ray range. Maximally rotating BHs produce continua which are harder those of non-rotating BHs, but they do not solve the problem either.

2. The local BB gives the correct result at optical to near-UV wavelengths (this would not be true for the UV band and for higher masses[43]), and confirms *our previous conclusion that the time-delay observed between the optical and UV bands is too small compared with the smallest time-scale in the disk.*

Hubeny and collaborators[41,42,43] solved self-consistently the vertical structure with an exact radiative transfer with no diffusion and escape probability approximation, in the non LTE case, taking into account the general relativistic transfer function. However, they did not take into account Comptonization, or heavy elements, so their models probably do not correctly describe the EUV. They computed the most extensive set of models to date: a grid of non-LTE disks around maximally-rotating Kerr and Schwarzschild BHs, for a wide range of BH masses and accretion rates. Some of their results are shown in Figs. 12, 13, and 14.

Figure 12. Spectral energy distribution of an α-disk around a maximally rotating BH (solid lines) and a Schwarzschild BH (dashed lines), with $M = 10^9$ $M_\odot$ and various values of the accretion rates. The curves correspond to $L/L_{\rm Edd}$= 1, 1/2, and 1/4, etc., for the Kerr BH; and the corresponding values for the Schwarzschild BH are 5.613 times larger. From Hubeny et al.[43]

Figure 13. Optical/ultraviolet spectral slope between 1450 and 5050Å for an α-disk around a Kerr BH with 37^o viewing angle, and $\alpha = 0.01$. Solid curves: computed models; dashed curves: local BB. From top to bottom, the curves are computed for 9 values of M: 1/8, 1/4, 1/2, 1, 2, 4, 8, 16, and 32 $\times 10^9 M_\odot$. From Hubeny et al.[43]

Figure 14. Lyman edge strength as a function of Eddington ratio for an α-disk around a Kerr BH with $M = 10^9$ $M_\odot$. The curves are labelled with the value of $\cos i$. From Hubeny et al.[43]

Fig. 12 compares the energy distributions of disks of Schwarzschild and Kerr BHs of 10^9 $M_\odot$ viewed at 37^o, for different disk luminosities. Schwarzschild and Kerr BHs produce quite similar optical spectra, except that in Kerr BHs the spectrum is shifted towards higher frequencies.

Fig. 13 displays 1450 to 5050 Å spectral slopes, β (defined here as $F_\nu \propto \nu^\beta$), as a function of the Eddington ratio for Kerr BHs of different masses. The local BB models depart from real transfer models except for low accretion rates. This is due to the relatively high masses considered. Both sets of models can reproduce the mean observed colors of the LBQS sample[32]. However, one should note that *the models cannot account for the positive slopes observed in the majority of Seyfert galaxies*.

Finally, Fig. 14 shows the strength of the Lyman edge in a Kerr BH with different disk inclinations. The Lyman discontinuity is always more intense than observed, except for very low accretion rates or very large disk inclinations, not plausible in the framework of Unification. It is however possible that the addition of metal opacity (not taken into account in the computations) changes this result.

This discussion illustrates the fact that the computation of disk spectra is difficult and involves poorly known parameters. Besides, several other parameters not mentioned here complicate the problem, such as the value of α, the

Figure 15. Sketches of several models of irradiated disks (the lamppost, the disk-corona, the patchy corona), and of the cloud model.

inner and outer radii of the disk, the different assumptions concerning heat deposition, etc. Therefore, in some cases it may not be a bad choice to use the simplest and least model-dependent solutions. Despite these uncertainties, the following results can be considered as secure:

- the spectral energy distribution does not fit the observations in the soft X-ray range: another emission mechanism is required;
- the disk spectrum in the optical to near-UV range is too flat compared to that of many Seyfert nuclei;
- the computed Lyman discontinuity is too strong or has to be fine-tuned;
- the small or absent time-lag between the optical and UV bands is not compatible with the viscous time-scale, or even with the dynamical time;
- the disk is not emitting hard X-rays at all.

Additionally, we paid no attention to polarization properties. They are also hard to explain in the context of the standard disk model.

8 Other Disk Models

8.1 The "Lamppost" Model

The discussion on the standard disk model has shown that the regions emitting at UV and optical wavelengths are located at large distances from each other, so the small time-lags between the (well correlated) optical and UV light curves require a causal link propagating at the speed of light. This led to questioning the validity of the thin steady disk model[7,21], and to propose that the disk was actually irradiated by the X-ray continuum, and emitting as a result of both gravitational and external radiative heating[17,83,106]. The discovery of the iron line and the X-ray hump[99] implied reprocessing by a cold medium, in agreement with this model.

There then followed the era of "irradiated disks". These models included an X-ray point source located at a given height A above the center of the disk, or a spherical source of radius A around the BH. The former is now referred to as the "lamppost model" (cf. Fig. 15).

The flux falling on each face of the disk $F_{\rm X}$ can be expressed as

$$F_{\rm X} = a f_{\rm X} \frac{L_{\rm bol}}{4\pi(R^2+A^2)} \cos\theta \sim f_{\rm X} \frac{L_{\rm bol} A}{4\pi R^3} \quad , \tag{51}$$

where $f_{\rm X}$ is the fraction of the bolometric luminosity emitted by this source, θ is the angle of the light rays to the normal, and $a = 1/2$ for a point source

and $a = 2/3\pi$ for a spherical source. The second approximation is valid for $R \gg A$, i.e. for the optical to near-UV emitting regions, located much further away than the X-ray source. X-ray variability studies suggest that $A \sim 10 R_{\rm G}$. *Therefore, the external flux varies with the radius like the viscous flux.* This external irradiation has several effects on the disk:

- A major fraction of X-rays is absorbed by photoelectric processes in the upper layers of the atmosphere, and this creates a hot and ionized "skin" which emits the iron line.

- The remaining fraction is Compton scattered in this ionized atmosphere and gives rise to the X-ray "hump".

- The absorbed fraction is reprocessed into UV, of which about 50% is re-emitted outwards and 50% towards the interior. This latter fraction can modify the internal structure of the disk. The effect is however negligible, unless $f_{\rm X} \approx 1$.

  Indeed, the condition for radiative heating to dominate the viscous heating when the disk is optically thick is[40,48]

  $$F_{\rm visc}\ (1 + \frac{3}{8}\tau_{\rm R})\ \leq \frac{F_{\rm X}}{2}\quad . \tag{52}$$

  Since this condition is not realized, the radial structure is not modified (unlike in the disk-corona model).

- The fraction of UV radiation re-emitted outwards is added to the emission due to the viscous flux.

The emitted spectrum has been computed using different schematizations. Except for the most recent ones[95], the models consist of a disk of constant density in the vertical direction, irradiated on the top by a power-law continuum and on the bottom by a BB (or by a Wien spectrum) to approximate the effect of viscous heating. The transfer is treated with various approximations[108,73,19,121] or with a Monte Carlo method coupled with a photoionization code[135]. An example is given in Figs. 16 and 17. Fig. 16 shows that iron is strongly ionized in the upper layers. The spectrum displayed in Fig. 17 illustrates the effects mentioned above. It is computed with the code TITAN[27], which solves the complete non-LTE transfer inside lines and continuum, with photoionization and thermal equilibrium, and is coupled to a Monte Carlo code to handle Compton diffusion. The strong UV-bump corresponds to the viscous release, to which a small ($\sim$ 10%) contribution

Figure 16. Ionization state of iron in the upper layers of an irradiated disk. The model is a slab of constant density 10^{14}cm^{-3}, irradiated on one side by a power-law $F_\nu \propto \nu^{-0.9}$ from 1eV to 100 keV and on the other side by a BB with $T = 10^5$K to mimic the viscous heating. The ionization parameter is $\xi = 300$, and the luminosity of the power-law is equal to the luminosity of the BB. Computations made with TITAN.

Figure 17. Emission spectrum for the same model as Fig. 16. The dotted line represents the underlying transmitted BB spectrum; the dashed line, the reflected spectrum; and the solid line, the total spectrum emitted by the disk. The spectral resolution (R) of the spectrum has been degraded to 30.

of reflected radiation is added. It is interesting to note that the Lyman discontinuity, present here in absorption, is quite weak, though not completely absent, as in the observed spectra. In the soft X-ray range the spectrum has a slope of the order of 1.5 in flux, in agreement with the observations, and displays many lines and edges from a highly ionized medium. Such lines are observed in the Chandra spectra of NGC 3783[54], and NGC 5548[52], unfortunately strongly blended with absorption lines from the Warm Absorber, and perhaps partly produced by it. This continuum is the "reflected" spectrum, though obviously it is not due to pure reflection! In the hard X-ray range an intense iron line is produced at 6.4 keV, due to Fe XVII and less ionized species.

This model is able to solve several problems raised by the standard non-irradiated disk model, like the presence of the soft X-ray excess, the iron line and of the "hump"; but it retains a few unsolved problems:

- Only a small fraction of the UV flux can be produced in this way as the X-ray luminosity is smaller than L(BBB). One deduces that the optical to UV emission is only slightly modified with respect to the standard disk (see also Fig. 17). Since the local BB picture holds for the optical to near-UV emission, one has $T_{\rm BB} = [(F_{\rm visc} + F_{\rm X})/\sigma]^{1/4}$, and therefore $T_{\rm BB} \propto R^{-3/4}$, except in the very central regions, where anyway the BB approximation is not valid and only EUV is emitted. Consequently to get a steep spectrum, $F_\nu \propto \nu^{-\alpha}$ with $\alpha \geq 0$ as observed in Seyfert nuclei, one should seek another geometry for the irradiation of disks.
- The disk will respond to a variation of the central source on a time-scale of $\sim\ 1.2\lambda_\mu^{4/3}\eta^{-1/4}f(R)^{1/4}\dot{m}^{1/4}M_8^{3/4}$ days, according to Eq. (21). Thus,

rapid X-ray fluctuations will be erased by the light travel-time towards the disk, as observed. But the UV–optical light curves should always lag behind the X-ray one, while the opposite is sometimes observed, for instance in the case of NGC 7469. Also the model cannot explain the fact that the UV light curve has the same variability amplitude as the X-ray with the characteristic UV time-scale.

- The problem of the Lyman discontinuity remains, although improved with respect to non-irradiated disk.
- Finally, the model requires the presence of an ad-hoc X-ray source for which no physical emission mechanism is proposed.

8.2 What Can We Learn about the Emitting Medium from the X-ray Spectrum?: Where Compton Scattering Makes its Appearence Again

We know that the X-ray spectrum is made of a reflected part (the "cold" iron line, the hump), and of a primary spectrum. The reflection takes place on a "cold" medium, which most probably is that emitting the UV-bump. The correlated variations and the small time-lag of the UV and X-ray fluxes confirm that the two emitting media are "seeing" each other. The high energy cut-off of the primary spectrum at about 100 keV tells us that it is emitted by a hot medium with an electron temperature such that $\Theta_e = kT_e/mc_o^2 \sim 0.1$ (if the emission is mainly due to electrons, which is most likely).

Three thermal mechanisms can compete in this hot medium: free-free, cyclotron, and inverse Compton emission. The time-scale for inverse Compton cooling is smaller than the time-scale for free-free cooling when the following inequality holds

$$l = \frac{L_{\rm UV}}{R}\frac{\sigma_{\rm T}}{mc^3} \sim 10^4\ \frac{L_{\rm UV}}{L_{\rm Edd}}\frac{1}{r} > 0.03\Theta_e^{-1/2} \sim 10^{-2}\quad , \tag{53}$$

where l is the "compacity" of the UV emission region.

The dimension of the UV emission region is typically $100R_{\rm G}$. One deduces that the condition is easily fulfilled, so inverse Compton cooling dominates over free-free cooling. It dominates also over cyclotron cooling unless the magnetic pressure is of the order of the density of radiation, which implies a very high value of the magnetic field. In conclusion: *the optical-UV and the X-ray emissions are probably strongly coupled through direct (in the cold medium) and inverse (in the hot medium) Compton scattering.*

In the hot Thomson thick medium there were multiple scatterings of hard photons. In the hot Thomson thin medium with soft photon input there is a small number of scatterings. This model was proposed for X-ray binaries[114].

The mean amplification per scattering is $A = 1+4\Theta_e - h\nu_0/m_e c^2$. If $\tau_{\rm T} < 1$, the probability of m scatterings is $\tau_{\rm T}^m$. After m scatters, $\nu/\nu_0 = A^m$. This creates a series of humps with decreasing intensities. One can thus approximate the Comptonized spectrum as a power-law $I(\nu) = I(\nu_0)(\nu/\nu_0)^{\ln(\tau_{\rm T})/\ln A}$. For a given energy of the soft photons, the spectral index is therefore defined by $\tau_{\rm T}$ and T_e. Moreover no photons can be scattered to an energy greater than that of the thermal electrons, and thus, one expects the power-law to be cut at $h\nu/kT_e \sim 1$.

Since the cooling of the hot gas is due to inverse Compton scattering, its temperature can be determined from an energy balance equation, provided that the heating is known, and thus one can completely determine the spectral distribution. This led to the introduction of a disk model where the release of gravitational energy occurs in a hot optically thin "corona" above the disk, through buoyancy and magnetic field reconnection[68,36,37]. If a large fraction ($f \sim 1$) of the gravitational release takes place in the corona, the disk is almost exclusively heated by the backscattered radiation coming from the corona. It reprocesses this radiation into a soft BB, and the corona upscatters this radiation while being Compton cooled by this process (cf. Fig. 15). This radiative coupling between the disk and the corona and the energy balance of the corona impose a relation between T_e and $\tau_{\rm T}$ (the smaller $\tau_{\rm T}$, the larger T_e), such that the X-ray spectral index is close to unity. Since an increase in $\tau_{\rm T}$ causes both a decrease of T_e and a steepening of the spectrum, a relation between the cut-off at high energy and the spectral index in the 2-10 keV range is predicted (cf. Fig. 18).

Since the ratio between the inverse Compton luminosity and the soft luminosity is of the order of unity, the model predicts a BBB/X-ray luminosity ratio smaller than observed. This is why a variant of the disk-corona model, the "patchy corona" (cf. Fig. 15), was introduced[38]. The corona is not homogeneous, but is made of a few blobs, which could be due to the formation of magnetic loops storing energy and releasing it rapidly through reconnection like in solar flares. Below a flare, the disk is heated to a higher temperature. The rest of the disk radiates through viscous processes. An important difference with the continuous corona is that the fraction of the disk located below the "flare" is much more irradiated and consequently its upper layers are strongly modified, in particular due to the large radiative pressure.

8.3 The Two-Phase Disk

In the previous model the gravitational release takes place mainly in the corona. This implies strong structural changes of the disk, both vertically

Figure 18. Comptonized spectra for different couples of $(\tau_{\rm T}, \Theta_e)$ [(0.63, 0.11), (0.32, 0.21), (0.2, 0.3), (0.1, 0.5)]. The soft photons correspond to a BB with $kT_{\rm BB}$ =100 eV. From Haardt et al.[39]

and radially, with respect to the standard model.

Disk-corona models have been studied in many papers[87,63,136,126,122,109,110]. Since the disk has no or only weak internal heat generation, it is almost isothermal and has a weak radiation pressure. It is therefore very dense and supported only by gas pressure. Consequently *it is not subject to the viscous/thermal instability like radiation supported disks*. This is a great advantage, but on the other hand, since these disks are very dense, they are gravitationally unstable at all radii for relatively modest luminosities. Other differences with the lamppost model is that the corona pressurizes the disk, and there is conductive transport between the disk and the corona.

Generally, the corona is a two temperature plasma, where ions are heated and transfer their energy to the electrons through Coulomb collisions, and the electrons are Compton cooled. The corresponding equilibrium temperature is close to virial for the ions (10^{11}K), and of the order of 10^9K for the electrons, as already mentioned. Therefore, the gas pressure supported corona is at the limit of being geometrically thick, and sometimes it is quasi-spherical. Some people think that a collective process able to rapidly transfer energy between ions and electrons can maintain the two constituents at the same temperature.

In these models, the fraction of energy generated in the corona is a free parameter given for instance[55] by a power-law in R. By changing this fraction and the geometry of the hot region, the models can fit the observed X-ray spectra. But one should search for a physical basis for the choice.

Some models take into account mechanical transport only in the radial direction, and others add the vertical transport by conduction or evaporation between the disk and the corona. Models with the local corona strength, calculated on the basis of the disk evaporation rate, tend to predict a relatively weak corona above a disk, with possible total disk disruption in its innermost part[110,76]. These results are supported by 2D numerical time-dependent computations[44]. However, these models do not predict strong the soft X-ray excesses present in composite spectra[65], as Comptonization in the corona is too weak and the emission from the innermost single phase flow arises in the hard X-ray part of the spectrum.

8.4 The Iron Line: a Proof for Irradiated Cold Relativistic Disks?

When an X-ray photon is absorbed to eject one of the two K-shell electrons of an iron ion, this photoelectric process is followed by the de-excitation of an electron from the L-shell, and then, either by the emission of a "fluorescent" K-photon, or by a subsequent Auger ionization (escape of an electron from an upper shell without emission of radiation). The probability of these two processes is of the same order and depends slightly on the ionization state of the ion. The energy of the fluorescent photon is almost constant and equal to 6.4 keV for Fe I to XVII, then it increases to 6.9 keV for the H-like Fe XXVI. Actually this transition and the one corresponding to the He-like Fe XXV are not "fluorescent" but simply normal resonance Lα transitions. Besides, from Li-like (Fe XXIV) to H-like iron, the Auger effect cannot occur, owing to the lack of two electrons in the L-shell. The absorption threshold is 7.1 keV for photoionization of a neutral atom, and it increases to 8 keV for Fe XVII, to reach 9.3 keV for Fe XXV.

The ionization state of iron depends on the ionization parameter ξ. For constant gas density one finds[73,74]:

for $\xi \leq 100$**:** a "cold" line is produced at 6.4 keV by ions less ionized than Fe XVII, and the iron K-shell absorption edge is small since the contribution of the other elements to the photoelectric opacity is large.

for $100 < \xi \leq 500$**:** iron is in the states Fe XVII to Fe XXIII. There is a vacancy is the L-shell of the ion, so Kα photons are resonantly absorbed and trapped until they disappear by the Auger effect. Only a few line photons can escape and the Fe K line is very weak. The lower-Z elements are ionized, leading to a moderate iron absorption edge.

for $500 < \xi \leq 5000$**:** the line photons are still subject to resonant scattering, but since they are not destroyed by the Auger effect they can escape the disk and produce an intense "hot" iron line at 6.8 keV. The absorption edge is strong.

for $\xi > 5000$**:** iron and the other elements are completely ionized, so there is no line and no edge.

As we shall see in the next section, *this is no longer valid for a constant pressure medium or for a disk in hydrostatic equilibrium.*

The flux of the line and the strength of the ionization edge depend on the ionization state, but also on the iron abundance, the geometry of the reprocessing medium, and, in the case of a plane-parallel slab, on the inclination of the line of sight and the illuminating source itself. We shall not

Figure 19. Profile of the iron line emitted by a disk around a Schwarzschild and a maximally rotating Kerr BH. The disk is assumed to extend down to the last stable orbit. From Fabian et al.[31], ©2000, Astr. Soc. of the Pacific, reproduced with permission of the editors.

give here more details about these dependences (see Fabian et al.[31]). The observed mean intensity, centroid energy, and equivalent width, lead to the conclusion that the line is produced in a relatively "cold" medium (meaning that iron is less ionized than Fe XVII), covering about 2π steradians of the central source (therefore an infinite slab irradiated by an X-ray source is an acceptable geometry).

It is widely accepted that the line profile is a proof of the formation of the line at the surface of the accretion disk, very close to the BH. The extended red wing is then due to gravitational redshift, while the blue wing is relativisticaly boosted due to the large rotational motion. As an illustration, Fig. 19 displays on the left the profile of the line emitted by a disk around a Schwarzschild BH extending from 6 to $30R_{\rm G}$, as a function of the inclination of the disk. The intensity of the blue wing depends strongly on the inclination. The figure on the right compares the profile of a line formed in an accretion disk around a Schwarzschild and a Kerr BH, for an inclination of 30^o. In the case of the Kerr BH, the disk is assumed to extend down to $1.25R_{\rm G}$, so the gravitational redshift is stronger and the red wing is more extended.

Fitting the profile of the line in several objects led to a number of surprising results. First the absence (or the weakness) of the blue wing corresponds to an inclination close to 30^o. Second, at least in the two best observed objects, NGC 3615 and MCG-6-30-15, the disk should extend down to $2R_{\rm G}$ to account for the broad red wings. Fabian et al.[31] argued against Reynolds & Begelman[103] for a Kerr geometry, as the gas falling inside the last stable orbit on a Schwarzschild BH would be highly ionized and the spectrum would display a strong absorption edge, inconsistent with the observed data.

8.5 More Realistic Computations of the Emission Spectrum

A first attempt to compute the emission of a disk topped by a corona in a consistent way was made by Sincell & Krolik[121]. Their transfer method was already mentioned in the discussion of the standard disk. They relaxed the condition of constant density, and solved the coupled vertical structure (i.e. hydrostatic equilibrium of the irradiated layer) and the radiation transfer, assuming that the energy release takes place entirely in the corona. The

Figure 20. Comparison between the temperature structure of an irradiated layer for constant density and for constant pressure. The curves are labelled with the log of the flux incident on the layer. The constant density layer and the surface of the constant pressure layer have a density 10^{12} cm^{-3}, the incident spectrum is a power-law with a spectral index unity, from 0.1 eV to 100 keV. Computations made with TITAN.

density in the X-ray heated skin is very high ($\sim 10^{18}$ cm^{-3}) and justifies their LTE approach. Integrating the emission over the radius, they computed the UV continuum emitted by the X-ray heated skin. Their calculations predict a strong Lyman discontinuity in emission, in strong disagreement with the observations.

Nayakshin and collaborators[95,96] also solved consistently the radiation transfer, with a complete treatment of the ionization and thermal equilibrium (not limited to H and He) and the hydrostatic equilibrium of an irradiated disk, not restricted to the case of a strongly pressurizing corona. They stressed that *hydrostatic equilibrium is extremely important for the structure of the ionized skin*, owing to the the thermal instability mechanism linked with the Ξ vs. T curve (cf. Fig. 4): when the temperature reaches the unstable part of the curve, it "jumps" to the other stable part. In contrast with the constant density case, which predicts a smooth decrease of the temperature with increasing depth inside the irradiated layer, hydrostatic equilibrium predicts a sharp transition between the hot and the cold stable phases. The same phenomenon occurs in the constant pressure case, as shown in Fig. 20. One also sees that the hot layer is thicker in the constant density case, owing to the rapid increase of density. As a consequence, for constant pressure the spectrum displays a UV-bump restricted to a one temperature BB, while for constant density the UV-bump is much more extended in frequency, and it joins smoothly the soft X-ray range (cf. Fig. 21). Fig. 22 shows that for constant density, no "cold" iron is present, unlike in the constant pressure case, where the cold layers are closer to the surface, so the soft photons emitted by these layers are able to leave the medium.

For hydrostatic equilibrium, the emissivity of the line and the spectral distribution of the continuum reprocessed in the atmosphere of an irradiated disk depends strongly on a dimensionless "gravitational parameter" A, proportional to the ratio of the gravity to the radiation pressure term[95,96,94]. Fig. 23 shows that for constant density, when the iron line is intense, it is always highly ionized. For hydrostatic equilibrium (which isi referred to as the self-consistent case), when the iron line is intense, it is a "cold" line. This

Figure 21. Comparison between the spectrum reflected by an irradiated layer for constant density and for constant pressure. Same density and incident continuum (the dotted line) as in Fig. 20.

Figure 22. Zoom of Fig. 21. Computation made with TITAN and NOAR.

Figure 23. Comparison of the constant density case with the hydrostatic equilibrium case ("self-consistent case"). The curves are labelled with ξ in the first case and with the gravitational parameter A in the second case. One sees that the iron line is "cold" in the self-consistent case, and "hot" in the constant density case. From Nayakshin et al.[95]

might explain the predominance of "cold" iron in AGN spectra. The observed correlations are better accounted for by a strong illumination of the disk, corresponding to the "patchy" or "flaring" corona model, than by the lamppost or the continuous corona[96]. Clearly more of these self-consistent computations (unfortunately enormously time consuming) are needed to get a real physical understanding of the complex observed behavior of AGN spectra.

9 An Alternative to the "Cold Relativistic Disk"? The "Cloud Model"

The iron line and UV continuum are both due to reprocessing of the X-ray continuum, for instance in the atmosphere of an irradiated disk. Hence the regions contributing the most to the variable fraction of the UV flux should give rise to an iron line, and inversely the region emitting the iron line should produce a UV or a EUV excess of continuum emission.

We have seen that the optical-UV variable continuum is emitted at large distances from the BH (at $R \sim 100$ to 1000 $R_{\rm G}$), with the result that a fraction of the iron line is also reprocessed in this region. The iron emission will appear as a narrow line at 6.4 keV, constant on UV variation time-scales. It is not clear whether a narrow core is always observed, but we know that the broad-line stays constant on time-scales of the order of days while the underlying X-ray continuum varies. Also there seems to be a contradiction between the short time-lag of the optical and UV light curves and the relative large time-

lag between the UV and the X-ray light curves. Generally speaking both the iron line and the optical-UV-X observations, in particular their variability properties, have been surprising in the context of the disk model.

An alternative geometry has been proposed[35,12,62], where the Fe K line and the UV continuum may arise from dense clouds (optically thick for free-free absorption, but not Thomson thick) with a large covering factor embedded in a hot quasi spherical medium, rather than from a disk. A variant of this model, with Thomson thick clouds, has also been proposed[18]. Fig. 15 displays a sketch of the "cloud model". In this model Compton scattering broadens the iron line.

A physical basis for the model can be found in a new inhomogeneous equilibrium of the disk where the bulk of the mass rests in dense clumps magnetically connected in a bath of hot gas[58]. One advantage of the model is that it is thermally and viscously stable. The transport of angular momentum is insured by collisions between clumps. The requirements for dynamical and thermal equilibrium determines the parameters of the system, for example the temperature of the hot gas and the optical thickness (quite similar to that of the corona in the disk-corona model) of the clumps which are Compton thick with a covering factor close to unity.

Another possibility exists in the framework of a nuclear wind. There are several theoretical arguments for the existence of hydrodynamic winds or radiation-driven flows close to the BH. On the other hand, the fact that the UV and soft X-ray absorption lines are blueshifted is observational evidence for an outflowing medium. One can thus imagine that the quasi-spherical medium invoked in this model is simply the basis of the Warm Absorber, for instance similar to the wind envisioned by Murray & Chiang[85]. One interesting aspect of such a model is that the iron line would be easily redshifted by the Doppler effect from the position of the Fe XXV or Fe XXVI line (6.7 keV) to 6.4 keV or less, since the observer would be seeing a line emitted only from the illuminated side of the clouds.

This model is able to account for the UV-X spectrum of AGN[18,19,24]. The observed X-ray continuum is then a mixture of the primary continuum and of the continuum reflected by the illuminated side of the clouds, while the BBB is produced both by intrinsic emission of the clouds heated by the X-ray source and by reflection on the illuminated side of the clouds. Similar to the disk-corona model, the X-ray source can be the result of Compton upscatterings of the UV photons emitted by the surrounding clouds. The radius of the cold medium is $r \sim 40 \dot{m} n_{14}^{-1/2} M_7^{-1/2} \xi_3^{-1/2}$, where n_{14} is expressed in units of 10^{14} cm^{-3} and ξ_3 in 10^3. Fig. 24 shows an example of the spectrum obtained for such a model.

Figure 24. Spectrum emitted by a spherical shell of clouds surrounding a hot medium that upscatters the UV photons emitted by the irradiated clouds. The covering factor of the clouds is 0.9, and the ratio of the radius of the hot and cold media is 0.4. Spectrum computed with TITAN and NOAR. The noise in the right-hand side is a numerical artifact of the Monte Carlo method. The spectral resolution of the left-hand side is 100.

Figure 25. Amplification factor due to multiple reflections in the cloud model, assuming that the X-ray source is point-like. Starting from $\xi = 3000$, the effective primary ionization parameter illuminating the clouds reaches $\xi = 10880$. The covering factor of the clouds is 0.9, and the primary spectrum is a power-law with a spectral index equal to unity between 0.1 eV and 100 keV. From Abrassart & Dumont[3].

Figure 26. Fit of the mean iron line profile with the cloud model. The incident spectrum on the reprocessing shell is a power-law with unity spectral-index between 0.1 eV and 100 keV, the covering factor is 0.9, and the shell contains highly ionized ($\xi = 10000$) and nearly neutral ($\xi = 300$) clouds in equal proportion. From Abrassart & Dumont[3].

In this closed geometry the UV photons which are not upscattered to the X-ray range by clouds in the hot medium, undergo multiple reflections which amplify the UV-bump. Consequently the clouds "see" a spectrum richer in soft photons than the observer (cf. Fig. 25). This leads to a small Compton temperature of the clouds, which is important to account for Compton downscattering of the iron line photons (cf. below).

Such a medium has the power to Compton-broaden the iron line[23]. There are actually two possibilities[84]:

- the hot medium is surrounded by a cold Compton thick medium, so the iron line and the hump are emitted by the Comptonizing medium itself (Comptonization by reflection)[3];

- the iron line is intrinsically narrow because it is emitted at $\sim 100 R_{\rm G}$ from the BH, and it is Compton broadened when crossing a surrounding ionized Compton thick medium (Comptonization by transmission)[81,82,4].

An example of the model fit of the mean AGN spectrum[89] with Comptonization by reflection is shown in Fig. 26. Two types of clouds are required: "cold" clouds, which emit the "cold" component of the iron line, and highly ionized clouds, which insure Comptonization of the iron line. The BBB is produced by both media[3].

An interesting aspect of Comptonization by transmission is that it can account not only for the broad red wing of the iron line, but also for the

Figure 27. Profile of an intrinsic cold narrow 6.4 keV iron line, transmitted through an extended shell of Thomson depth 3, with a density varying as $1/R^2$ and $\xi = 2 \times 10^6$. The incident spectrum is a composite AGN[65]. From Abrassart & Dumont[4].

Figure 28. Same as in Fig. 27, but showing the effect on an extrinsic Lyman edge in absorption. From Abrassart & Dumont[4].

absence of a Lyman discontinuity in the UV spectrum without appealing to a fine tuning of the parameters (cf. Fig. 28).

The transmission model has been rejected[30,104] based on the size given by variability. The very high ionization state required to avoid an intense iron absorption edge implies too large a dimension, in particular in the case of MCG-6-30-15. However, assuming that the Comptonizing medium is homogeneous (the most conservative case), one deduces from Eq. (6) assuming $\xi = 10^6$ and $\tau_{\rm T} \sim 3$ a dimension of 0.03 lt-d, consistent with variability timescales. It corresponds to a distance of about $100R_{\rm G}$ if the BH in MCG-6-30-15 has a mass of a few $10^6 {\rm M}_\odot$, as it is now believed (note that such a small mass implies that this object is radiating close to its Eddington luminosity, making it peculiar among Seyfert nuclei). However a serious argument against the transmission model, is that the energy cut should take place at 500 keV / τ^2, i.e. at about 50 keV, while it seems to be observed above 100 keV.

A strong argument against the reflection model is the fact that it still has not been shown able to account for a very extended red wing with no blue wing, as observed in MCG-6-30-15. However the parameter space is far from having been completely explored, as these computations are extremely time consuming.

The main difference with the disk model is that the region where the iron line is emitted has not to be located close to the BH. This is in agreement with the absence of short term variations of the line strength correlated with variations of the continuum (though the rapid variations of the profile are difficult to account for except with an ad hoc geometry). It allows also for the UV and optical emission to arise at similar distances, of the order of $100R_{\rm G}$. On the other hand, in this model the clouds can randomly obscure the line of sight, thus accounting for short term variations of the primary X-ray source[5]. Another major difference with the disk model is that it also explains naturally a large $L_{\rm UV}/L_{\rm X}$ ratio, owing to the large covering factor of the "cold" medium.

Note that this model is in a sense "non local", as the cloud system can be compared to a photosphere which is reprocessing the gravitational energy that is emitted much closer to the BH.

Finally an intermediate solution has been proposed[53] where a system of quasi-spherically randomly keplerian moving clouds is located relatively close to the BH. In this scenario the iron line is broadened both by relativistic effects and by Comptonization.

10 And What Happens at the Largest and at the Smallest Accretion Rates? The Case for Thick Disks.

Up to now we have concentrated on accretion rates similar to those observed in Seyfert nuclei and modest quasars, where geometrically thin disks are a natural solution of the α-prescription. It is interesting to consider what happens at both higher and lower accretion rates, where thick disks are predicted.

In thin disks, vertical motions and radial pressure gradients are negligible, and it is therefore possible to neglect the flux advected towards the center,

$$F_{\rm adv} = \frac{\dot{M} c_{\rm s}^2}{4\pi R^2}\ f(R) \left(\frac{d\ln P}{d\ln R} - \frac{5}{2} \frac{d\ln T}{d\ln R} \right) \quad . \tag{54}$$

When the disk is geometrically thick, the radial velocity is comparable to the rotational velocity, and this induces strong radial pressure and temperature gradients. The advected flux must then be taken into account,

$$F_{\rm visc} = F_{\rm cool} + F_{\rm adv} \quad , \tag{55}$$

where $F_{\rm cool}$ is the heat flux radiated away. Let us consider the two extreme cases:

1. for $\dot{m} \gg$ or ~ 1: Owing to the large accretion rate, the flow is dense and optically thick, the inner regions are thus supported by the strong radiation pressure. Consequently, the disk is inflated and becomes geometrically thick. Heat advected to the BH exceeds the heat radiated away, and η decreases with $\dot{m}$ [1]. For super-Eddington accretion rates these disks have relatively small luminosities, of the order of $L_{\rm Edd}$. They radiate mainly in the soft X-ray range and it is suggested that they could account for Narrow Line Sy 1s, which probably radiate near their Eddington limit, and display large soft X-ray excess[79].

2. for $\dot{m} < \alpha^2$, i.e. typically ≤ 0.01: Owing to the small accretion rate, the flow has a low density and does not radiate efficiently. Like the coronae discussed previously, the protons remain very hot and the disk

Figure 29. Spectrum of an ADAF with a cold disk. The 4 curves correspond to different positions of the transition between the ADAF and the cold disk: infinity (no cold disk, pure flat ADAF spectrum), 1000 $R_{\rm G}$, 100$R_{\rm G}$, 10$R_{\rm G}$. The importance of the blue bump and its peak frequency increase when the transition radius decreases. Courtesy J.-P. Lasota.

is supported by gas pressure, becoming geometrically thick and optically thin. Several cooling processes can dominate whether or not soft photons are present to induce inverse Compton cooling[50,92,2,93]. Since these disks are not efficient radiators, a large fraction of the gravitational energy will be advected towards the BH and simply "swallowed". These disks are referred to as "Advection Dominated Accretion Flows" (ADAFs). Both solutions (i.e. the standard disk and the ADAF) exist, without any understanding on how to switch between them. If the ADAF is surrounded by a cold disk the emission spectrum will depend on the location of the transition between the cold disk and the ADAF (cf. Fig. 29). In this case the hot medium constituting the ADAF can be cooled by inverse Compton scattering of the soft photons produced by the cold disk. If a nuclear radio source is present, the synchrotron photons can play the same role in cooling the hot gas.

Much recent attention has been devoted these last years to ADAFs. They are generally thought to be present in low luminosity objects, such as LINERs and the nuclei of elliptical galaxies (M 87[102]), the nucleus of NGC 4258[66], and the Galactic Center[77]. All show a non-resolved X-ray source but no optical/UV continuum, as one expects from an ADAF. The theoretical possibility of an ADAF is a matter of current debate, and observationally it is controversed (in particular for Sgr A*[6]).

11 A "No Man's Land": the Disk between 10^3 and 10^6 $R_{\rm G}$

We have seen that the disks become gravitationally unstable beyond a few $10^3 R_{\rm G}$. Moreover, the viscous time-scale given by the α-prescription for transporting the gas towards the BH at such distances is larger than the lifetime of the active nucleus. We know that further from the center, at about 10^6 $R_{\rm G}$, the disk is globally gravitationally unstable and the supply of gas can be achieved by gravitational torques (cf. F.Combes in these lecture notes). However we know nothing about the structure of the disk in the intermediate region and how the outward transport of angular momentum is ensured.

Several solutions have been proposed. A magnetic field anchored in the disk can transport angular momentum non-locally, and possibly prevent gravitational instability. Another solution consists of a disk made from marginally unstable and randomly moving clouds with large bulk velocities, where the transfer of angular momentum is provided by cloud collisions[11]. A more elaborate model is proposed for NGC 1068[61] in which a disk of gas clumps undergoes mutual gravitational interactions. These disks would be geometrically thick, and are actually similar to the tori invoked in the Unified Scheme.

The observations of purely keplerian velocities in masers lying at about 10^5 $R_{\rm G}$ from the BH in NGC 4258[97] argue strongly for a geometrically thin warped disk. Collin & Zahn[20] have therefore adopted the view of a marginally stable disk where unstable clumps collapse until protostars are formed. (However, such a picture is only well suited for low Eddington ratios. For large Eddington ratios the number of newly formed stars is high, and the disk will become highly turbulent and inhomogeneous.) Stars embedded in an accretion disk should accrete at a high rate and rapidly acquire masses of a few tens of $M_\odot$, leading to a "starburst" of massive stars (not comparable in size with real starbursts)[9]. The mass transport can thus be driven by supernovae or by stellar outflows, which at the same time can contribute to the heavy element enrichment observed in the BLRs at high-z and in BALs. A larger scale starburst could also be induced in the shocked gas of supernova remnants. Several pieces of evidence have been discussed in these lectures for the existence of starbursts in the very central region of Seyfert galaxies.

Finally Ostriker[98] made a very interesting suggestion that has never been seriously considered. He stated that if the disk is embedded in a massive stellar system, interactions between the stars and the disk can remove angular momentum from the disk at the rate expected for an AGN.

12 Conclusion

It is not easy to conclude such a chapter because the results are really difficult to summarize. We have seen that the tremendous increase of data with the advent of X-ray missions such as ASCA, RXTE, and now Chandra and XMM, has considerably complicated the problem, and now precludes any simple interpretation. We have seen that the most detailed models, used to make observational predictions, are still based on crude approximations, such as geometrically thin, stationary and axisymmetric disks. For instance the models are generally assumed to be steady-state, despite the evidence that there exist strong variations on small time-scales. The viscosity is currently parametrized by the α-prescription, but other prescriptions are not excluded.

There are heated debates about the value of α, whether it is constant or not, whether the stress tensor is proportional to the total pressure or to the gas pressure. We don't know the influence of the magnetic field. We have no idea of the geometry of the inner regions. We know that there is a quasi-spherical hot accretion flow, but at the same time we believe that the cold thin disk extends down to a few gravitational radii from the BH, and in this case we know that it should be unstable. The status of the hot flow is not clear yet. In short, one could say that the more sophisticated the models, the larger the uncertainties! To continue to make progress, we must obtain very good new observational data, and at the same time develop the basic physics and tools for the modeling. The field has still a promising future in the third millenium!

Acknowledgments

I am grateful for enlighting discussions with B. Czerny, A-M. Dumont, J-M. Huré, M. Mouchet, and J-P. Zahn and to I. Aretxaga for a careful reading of the manuscript, leading to many clarifications and improvements.

References

1. Abramowicz, M.A., Calvani, M., Nobili, L., ApJ, 242, 772, 1980.
2. Abramowicz, M.A., Chen,X., Kato, S., Lasota, J.-P., ApJ, 438, L37, 1995.
3. Abrassart, A., Dumont, A.-M., Proc. of the First XMM workshop on "Science with XMM", M. Dahlem (ed.), 1998.
4. Abrassart, A., Dumont, A.-M., Proceedings of the Bologna Conference on "X-ray Astronomy, Stellar Endpoints, AGNs and the Diffuse X-ray Background" (Astroph. Lett. and Comm.), 1999.
5. Abrassart, A., Czerny, B., A&A, 356, 475, 2000.
6. Agol, E., ApJL, 538, L121, 2000.
7. Alloin, D., Pelat, D., Phillips, M. & Whittle, M., ApJ, 288, 205, 1985.
8. Antonucci, R. R. J., Miller, J.S., ApJ, 297, 621, 1985.
9. Artymowicz, P., Lin, D.N.C., Wampler, E.J., ApJ, 409, 592, 1993.
10. Balbus, S.A., Hawley, J.F., ApJ, 376, 214, 1991.
11. Begelman, M.C., Frank, J., Shlosman, I., in "Theory of Accretion disks", eds. F. Meyer et al., Kluwer Academic Publishers, 1989.
12. Celotti, A., Fabian, A.C., Rees, M.J., MNRAS, 255, 419 , 1992.
13. Chandrasekhar, S., Proc. Nat. Acad. Sci., 46, 53, 1960.
14. Chiang J., et al., ApJ, 528, 292, 2000.
15. Clarke, C.J., Shields, G.A., ApJ, 338, 32, 1989.
16. Collier, S.J., et al., ApJ, 500, 162 , 1998.

17. Collin-Souffrin, S., A&A, 249, 344, 1991.
18. Collin-Souffrin, S., Czerny, B., Dumont, A.-M., Zycki, P., A&A, 314, 393, 1996.
19. Collin-Souffrin, S., Dumont, A.-M., "Theory of Accretion Disks - 3", Eds E. Meyer-Hofmeister & H. Spruit, Springer, 1997.
20. Collin, S., Zahn, J-P., A&A, 344, 433, 1999.
21. Courvoisier, T., Clavel, J., A&A, 288, 389, 1991.
22. Czerny, B., Elvis, M., ApJ, 321, 305, 1987.
23. Czerny, B. & Zbyszewska, M., MNRAS , 249, 634, 1991.
24. Czerny, B., Dumont, A.-M., A&A, 338, 386, 1998.
25. Done, C., et al., MNRAS, 243, 713, 1990.
26. Doerrer, T., Riffert, H., Staubert, R., Ruder, H., A&A, 311, 69 , 1996.
27. Dumont, A-M., Abrassart, A., Collin, S., A&A, 357, 823 , 2000.
28. Edelson, R., Alexander, T., Crenshaw, D.M., ApJ, 470, 364, 1996.
29. Edelson, R., et al., ApJ, 534, 180, 2000.
30. Fabian, A.C, et al. 1995, MNRAS, 277, L11, 1996.
31. Fabian A.C., Iwasawa K., Reynolds C.S., Young A.J., PASP, 112, 1145, 2000.
32. Francis, P.J., et al., ApJ, 373, 465, 1991.
33. Frank J., King A.R., Raine D.J., "Accretion power in astrophysics", 2nd Ed., Cambridge University Press, 1992.
34. Goldreich P., Lynden-Bell D., MNRAS, 130, 97, 1965.
35. Guilbert, P.W., Rees, M.J. 1988, MNRAS, 233, 475, 1965.
36. Haardt, F., Maraschi, L., ApJ, 380, L51, 1991.
37. Haardt, F., Maraschi, L., ApJ, 413, 507, 1993.
38. Haardt, F., Maraschi, L., Ghisellini, G., ApJ, 432, L95, 1994.
39. Haardt, F., Maraschi, L., Ghisellini, G.,, ApJ, 476, 620, 1997.
40. Hubeny, I., ApJ, 351, 632, 1990.
41. Hubeny, I., Hubeny, V., ApJL, 484, L37, 1997.
42. Hubeny, I., Hubeny, V., ApJ, 505, 558, 1998.
43. Hubeny, I., Agol, E., Blaes, O., Krolik, J.H., ApJ, 533, 710, 2000.
44. Hujeirat, A., Camenzind, M., A&A, 361, 53, 2000.
45. Huré J-M., PhD thesis, University Paris 7, 1994.
46. Hure, J., A&A, 337, 625, 1998.
47. Huré, J-M., A&A, 358, 378, 2000.
48. Huré,J-M., Collin-Souffrin S., Le Bourlot J., Pineau des Forets G., A&A 290, 19, 1994.
49. Huré, J-M., Galliano , F., A&A, in press
50. Ichimaru, S., ApJ, 214, 840, 1977.
51. Iwasawa, K., Fabian, A.C., Reynolds, C.S., MNRAS, 282, 1038, 1996.

52. Kaastra, J.S., Mewe, R., Liedahl, D.A., Komossa, S., Brinkman, A.C., A&A, 354, L83, 2000.
53. Karas, V., Czerny, B., Abrassart, A., Abramowicz, M.A., MNRAS, 318, 547, 2000.
54. Kaspi, S., Brandt, W. N., Netzer, H., Sambruna, R., Chartas, G., Garmire, G.P. & Nousek, J. A. ApJL, 535, L17, 2000.
55. Kawaguchi, T., Shimura, T., Mineshige, S., ApJ, in press (astro-ph/0008404)
56. Kolykhalov, P. I., Sunyaev, R.A., High Energy Astrophysics and Cosmology, 249, 1984.
57. Koratkar A., Blaes O., PASP, 111, 1, 1999.
58. Krolik, J.H., ApJL, 498, L13, 1998.
59. Krolik, J.H., "Active galactic nuclei : from the central black hole to the galactic environment", Princeton University Press, 1999.
60. Krolik, J. H., McKee, C.F., Tarter, C.B., ApJ, 249, 422, 1981.
61. Kumar P., ApJ 519, 589, 1999.
62. Kuncic, Z., Celotti, A., Rees, M.J., MNRAS, 284, 717, 1997.
63. Kusunose, M. & Mineshige, S., ApJ, 423, 600, 1994.
64. Laor, A., Netzer, H., MNRAS, 238, 897, 1989.
65. Laor, A., Fiore, F., Elvis, M., Wilkes, B.J., McDowell, J.C., ApJ, 477, 93, 1997.
66. Lasota, J-P., Abramowicz, M. A., Chen, X., Krolik, J., Narayan, R., Yi, I., ApJ, 462, 142, 1996.
67. Lee, J.C., Fabian, A.C., Reynolds, C.S., Brandt, W.N., Iwasawa, K., MNRAS, 318, 857, 2000.
68. Liang, E.P.T. 1977, ApJL, 211, L67, 2000.
69. Lynden-Bell, D., Pringle, J.E., MNRAS, 168, 603 , 1974.
70. Malkan M.A., ApJ, 268, 582, 1983.
71. Malkan, M.A., Sargent, W.C.W., ApJ, 254, 122, 1982.
72. Mathews, W.G., Ferland, G.J., ApJ, 323, 456, 1987.
73. Matt, G., Fabian, A.C., Ross, R.R., MNRAS, 262, 179, 1993.
74. Matt, G., Fabian, A.C., Ross, R.R., MNRAS, 278, 1111 , 1996.
75. Meyer, F., Meyer-Hofmeister, E., A&A, 287, 559, 1994.
76. Meyer, F., Liu, B.F., Meyer-Hofmeister, E., A&A, 361, 175 , 2000.
77. Mezger, P. G., Duschl, W. J., Zylka, R., A&AR, 7, 289, 1996.
78. Mineshige, S., Shields, G.A., ApJ, 351, 47, 1990.
79. Mineshige, S., Kawaguchi, T., Takeuchi, M., Hayashida, K., PASJ, 52, 499 , 2000.
80. Misner, C. W., Thorne, K.S., Wheeler, J.A., San Francisco: W.H. Freeman and Co., 1973.

81. Misra, R., Kembhavi, A.K., ApJ, 499, 205, 1998.
82. Misra, R., Sutaria, F.K., ApJ, 517, 661, 1999.
83. Molendi, S., Maraschi, L., Stella, L., MNRAS, 255, 27, 1992.
84. Mouchet, M., Abrassart, A., Porquet, D., Dumont, A-M., Collin, S, to appear in "AGN in their Cosmic Environment", Eds. B. Rocca-Volmerange & H. Sol, EDPS Conf. Series in A&A, 2000.
85. Murray, N., Chiang, J., ApJ, 454, L105, 1995.
86. Mushotzky, R.F., Done, C., Pounds, K.A., ARAA, 31, 717, 1993.
87. Nakamura, K., Osaki, Y., PASJ, 45, 775, 1993.
88. Nandra, K., Large Scale Structure in the X-ray Universe, Proceedings of the 20-22 September 1999 Workshop, Santorini, Greece, eds. Plionis, M. & Georgantopoulos, I., Atlantisciences, Paris, France, p.249, 249, 2000.
89. Nandra, K., George, I.M., Mushotzky, R.F., Turner, T.J., Yaqoob, T., ApJ, 477, 602, 1997.
90. Nandra, K., et al., ApJ, 505, 594, 1998.
91. Nandra K. et al., ApJ, in press (astro-ph/0006339), 2000.
92. Narayan,R., Yi, I., ApJ, 452, 71, 1995.
93. Narayan, R., Mahadevan, R., Grindlay, J.E., Popham, R.G., Gammie, C., ApJ, 492, 554, 1998.
94. Nayakshin, S., ApJ, 534, 718, 2000.
95. Nayakshin, S., Kazanas, D., Kallman, T.R., ApJ, 537, 833, 2000.
96. Nayakshin, S., Kallman, T.R., ApJ, submitted (astro-ph/0005597).
97. Neufeld D.A., Maloney P.R., ApJL, 447, L17, 1995.
98. Ostriker, J.P., ApJ, 273, 99, 1983.
99. Pounds, K.A., Nandra, K., Stewart, G.C., George, I.M., Fabian, A.C., Nat, 344, 132, 1990.
100. Rees M.J., ARAA, 22, 471, 1984.
101. Reynolds, C.S., ApJ, 533, 811, 2000.
102. Reynolds, C. S., di Matteo, T., Fabian, A. C., Hwang, U., Canizares, C. R., MNRAS, 283, L111, 1996.
103. Reynolds, C.S., Begelman, M.C., ApJ, 488, 109, 1997.
104. Reynolds, C.S., Wilms, J., ApJ, 533, 821, 2000.
105. Richard, D., Zahn, J., A&A, 347, 734, 1999.
106. Rokaki, E., Collin-Souffrin, S., Magnan, C., A&A, 272, 8, 1993.
107. Ross, R. R., Fabian, A.C., Mineshige, S., MNRAS, 258, 189, 1992.
108. Ross, R.R. & Fabian, A.C. MNRAS, 261, 74, 1993.
109. Różańska, A., Czerny, B., Życki, P.T., Pojmański, G., MNRAS, 305, 481, 1999.
110. Różańska, A., Czerny, B., A&A, 360, 1170, 2000.
111. Rybicki, G.B., Lightman, A.P., New York, Wiley-Interscience, 1979.

112. Sanders, D.B., Phinney, E.S., Neugebauer, G., Soifer, B.T., Matthews, K., ApJ, 347, 29, 1989.
113. Shakura, N.I., Sunyaev, R.A., A&A, 24, 337, 1973.
114. Shapiro, S.L., Lightman, A.P., Eardley, D.M., ApJ, 204, 187, 1976.
115. Shields, G.A., Nat, 272, 423, 1978.
116. Shields, G.A., Coleman, H.H., Theory of Accretion Disks - 2, Kluwer Ed., 1994.
117. Shimura, T., Takahara, F., ApJ, 419, 78, 1993.
118. Shimura, T., Takahara, F., ApJ, 440, 610, 1995.
119. Shlosman, I., Begelman, M.C., ApJ, 341, 685, 1989.
120. Siemiginowska, A., Czerny, B., Kostyunin, V., ApJ, 458, 491, 1996.
121. Sincell, M.W. & Krolik, J.H., ApJ, 476, 605, 1997.
122. Sincell, M.W. & Krolik, J.H., ApJ, 496, 737, 1998.
123. Störzer, H., A&A, 271, 25, 1993.
124. Störzer, H., Hauschildt, P.H., Allard, F., ApJL, 437, L91, 1994.
125. Sun, W., Malkan, M. A., in "Astrophysical Jets and their Engines", 125, 1987.
126. Svensson, R., Zdziarski, A.A., ApJ, 436, 599, 1994.
127. Toomre A., ApJ 139, 1217, 1964.
128. Wandel, A., Petrosian V. ApJ 319, L11, 1988.
129. Wanders, I., et al., ApJS, 113, 69, 1997.
130. Weaver, K.A., Gelbord, J., Yaqoob, T., ApJ, in press (astro-ph/0008522).
131. Weinberg, S., "Gravitation and cosmology: Principles and applications of the general theory of relativity", New York: Wiley , 1972.
132. Zdziarski A.A., Lubinski P., Smith D.A., MNRAS, 303, L11, 1999.
133. Zdziarski A.A., Lubinski P., MNRAS, submitted (astro-ph/0009017).
134. Zheng, W., Kriss, G.A., Telfer, R.C., Grimes, J.P., Davidsen, A.F., ApJ, 475, 469, 1997.
135. Zycki, P.T., Krolik, J.H., Zdziarski, A.A., Kallman, T.R., ApJ, 437, 597, 1994.
136. Zycki, P.T., Collin-Souffrin, S., Czerny, B., MNRAS, 277, 70, 1995.

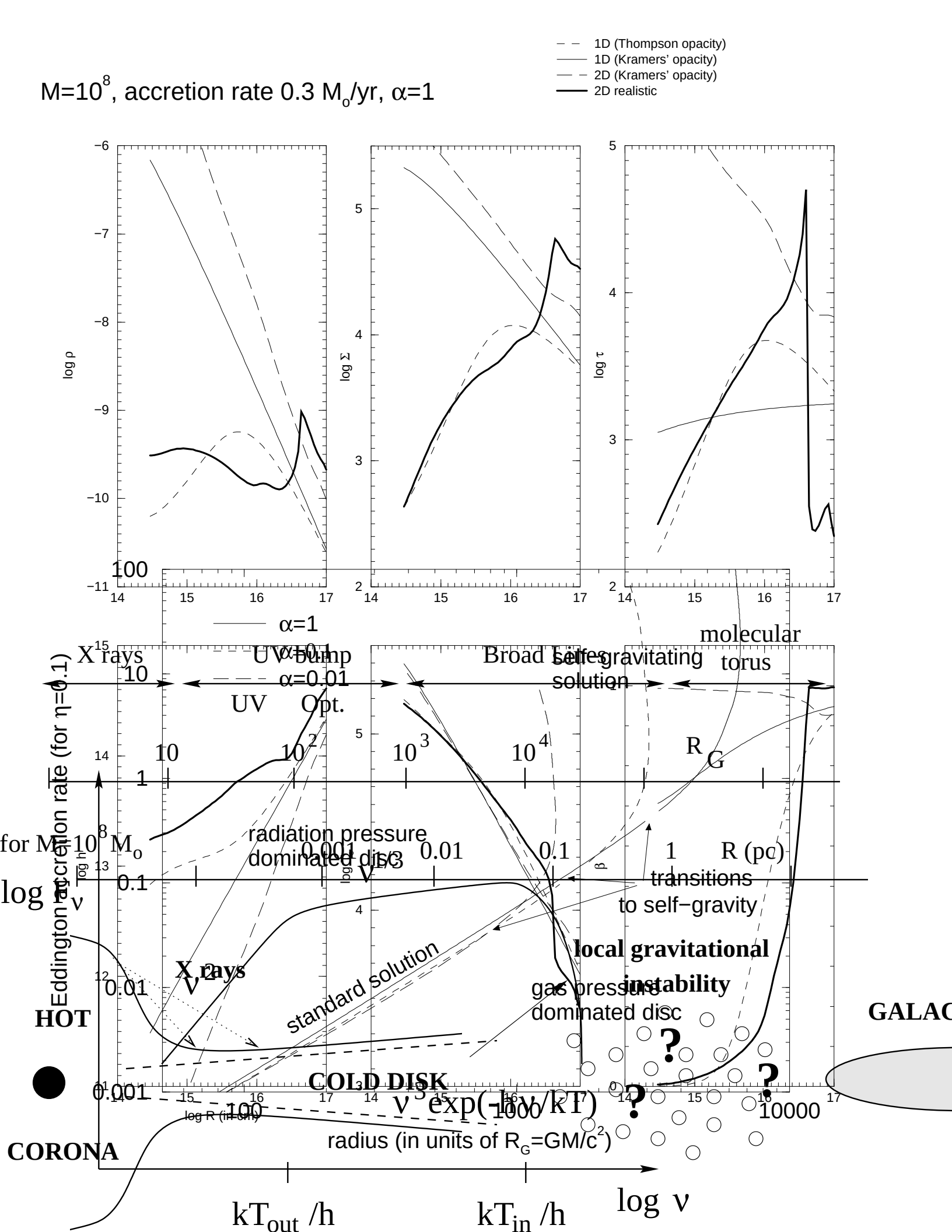
1D (Thompson opacity)
1D (Kramers' opacity)
2D (Kramers' opacity)
2D realistic
M=10^8, accretion rate 0.3 M_o/yr, α=1
log ρ
log Σ
log τ
100
α=1
α=0.1
α=0.01
X rays
UV Bump
UV Opt.
Broad Lines
self gravitating solution
molecular torus
10
1
0.1
0.01
0.001
R_G
R (pc)
β
log h
log T_c
log Eddington accretion rate (for η=0.1)
for M=10^8 M_o
log ν
radiation pressure dominated disc
ν^1/3
transitions to self−gravity
local gravitational instability
gas pressure dominated disc
standard solution
X rays
ν^2
HOT
COLD DISK
ν^3 exp(−hν/kT)
CORONA
GALAC
?
log R (in cm)
radius (in units of R_G=GM/c^2)
kT_out /h
kT_in /h
log ν

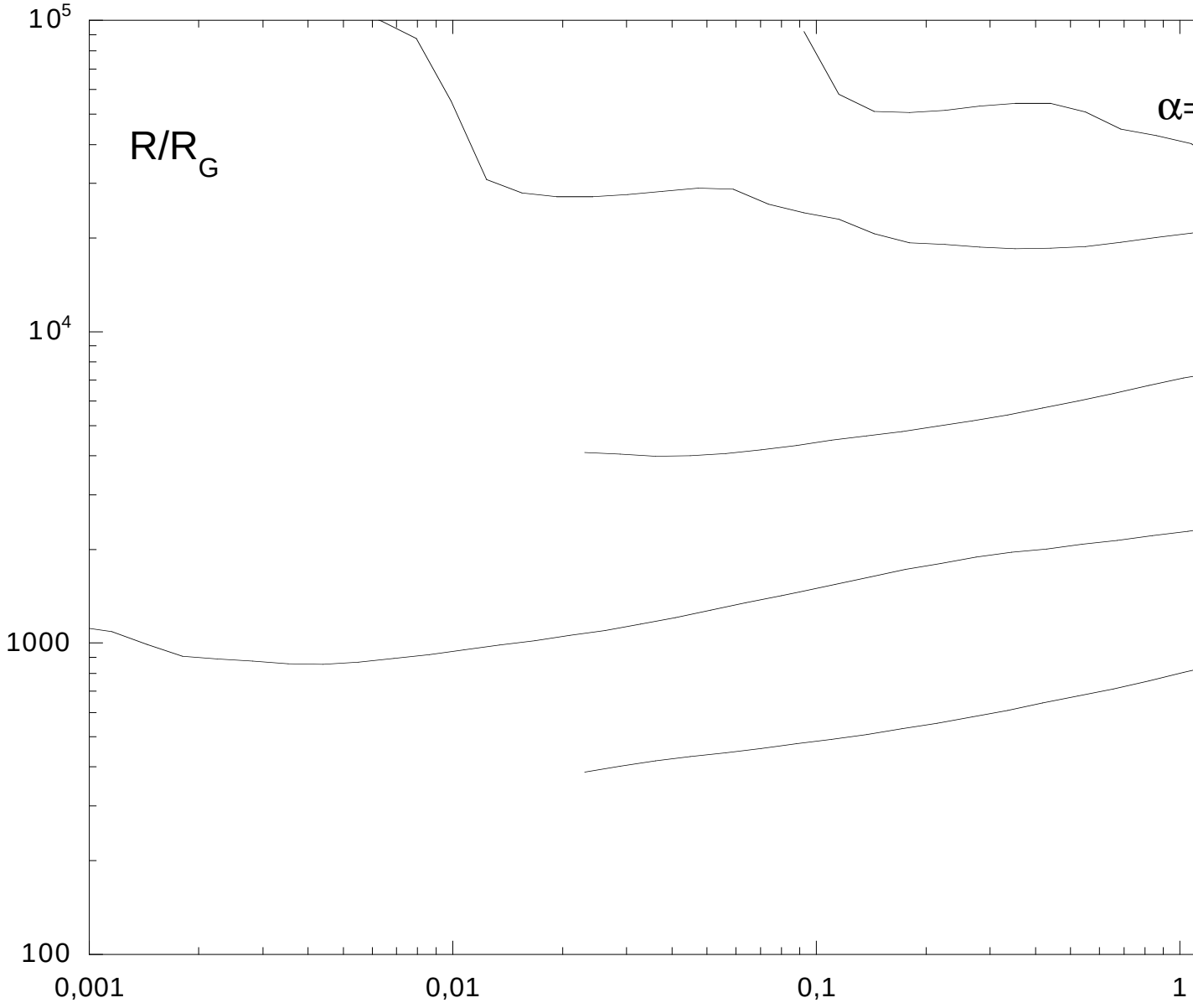
10^5
R/R_G
10^4
1000
100
0,001
0,01
0,1
1
α=

This figure "fig10a.png" is available in "png" format from:

http://arXiv.org/ps/astro-ph/0101203v2

This figure "fig11.png" is available in "png" format from:

http://arXiv.org/ps/astro-ph/0101203v2

This figure "fig14.png" is available in "png" format from:

http://arXiv.org/ps/astro-ph/0101203v2

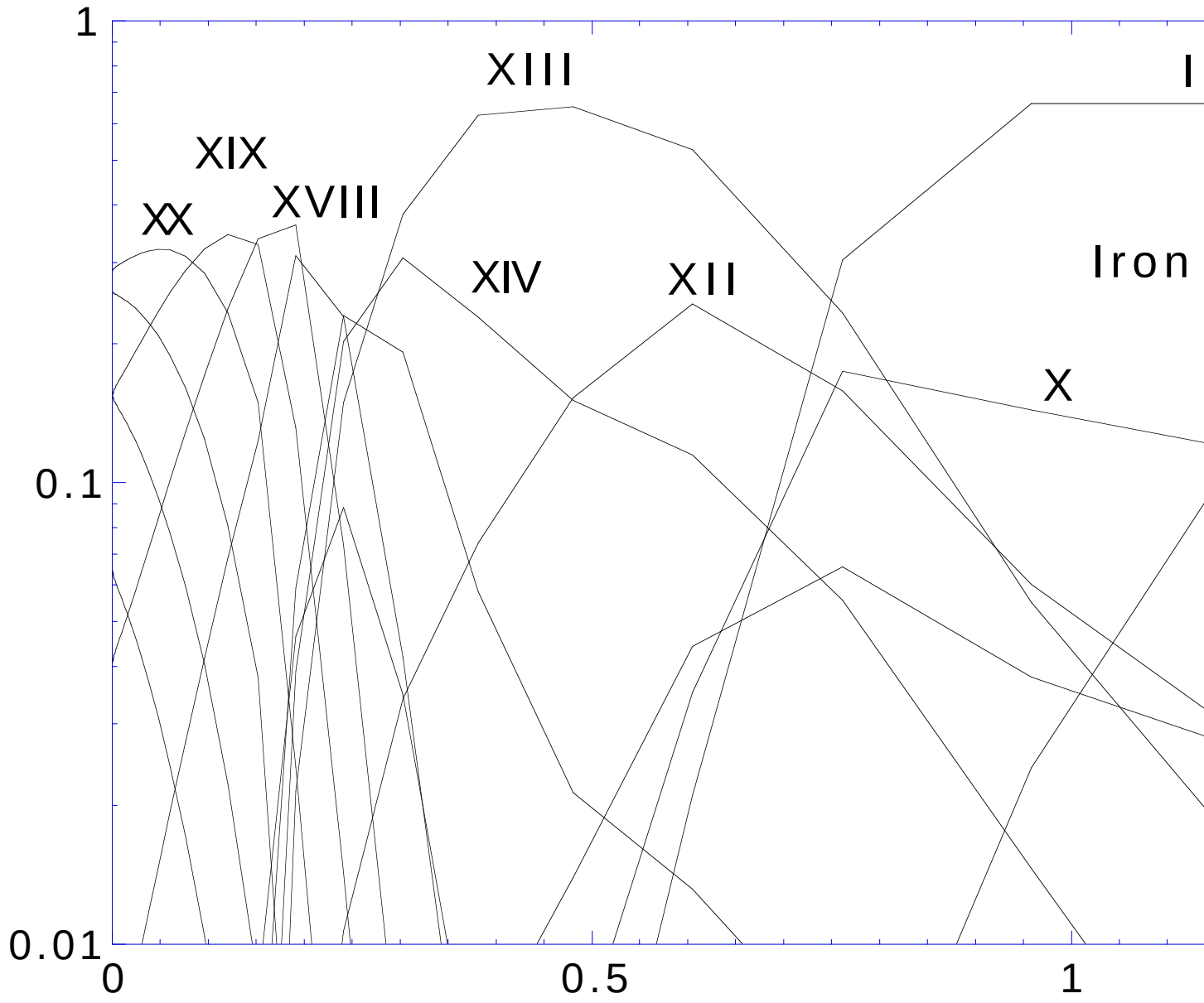
1
0.1
0.01
0
0.5
1
XIII
I
XIX
XVIII
XX
XIV
XII
Iron
X

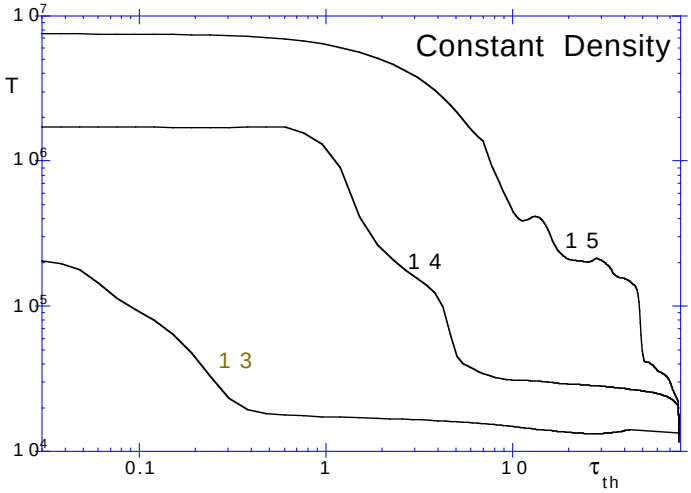
Constant Density
T
10^7
10^6
10^5
10^4
13
14
15
0.1
1
10
τ th

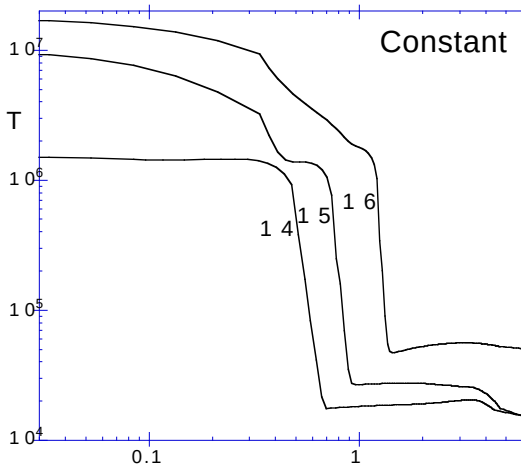
Constant
T
10^7
10^6
10^5
10^4
14
15
16
0.1
1

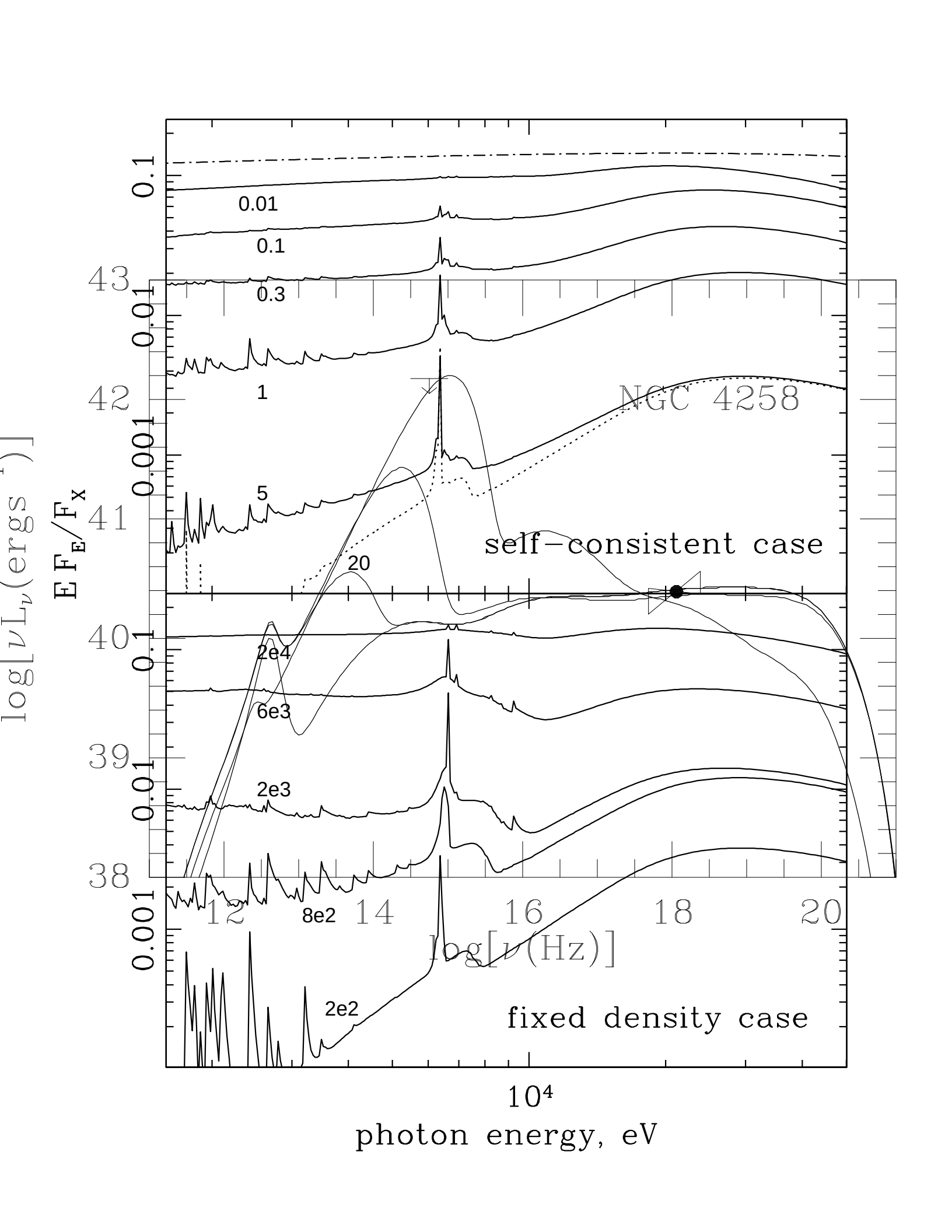
0.01
0.1
0.3
1
5
20
2e4
6e3
2e3
8e2
2e2
NGC 4258
self−consistent case
fixed density case
$E F_E/F_X$
$\log[\nu L_\nu(\mathrm{ergs}^{-1})]$
$\log[\nu(\mathrm{Hz})]$
photon energy, eV
10^4